

Cosmology with the SPHEREX All-Sky Spectral Survey

Olivier Doré^{1,2}, Jamie Bock^{2,1}, Matthew Ashby⁹, Peter Capak³, Asantha Cooray⁸, Roland de Putter^{1,2}, Tim Eifler¹, Nicolas Flagey¹¹, Yan Gong⁸, Salman Habib¹⁰, Katrin Heitmann¹⁰, Chris Hirata⁶, Woong-Seob Jeong⁷, Raj Katti², Phil Korngut², Elisabeth Krause⁴, Dae-Hee Lee⁷, Daniel Masters³, Phil Mausekopf¹², Gary Melnick⁹, Bertrand Mennesson², Hien Nguyen¹, Karin Öberg⁹, Anthony Pullen¹³, Alvis Raccanelli⁵, Roger Smith², Yong-Seon Song⁷, Volker Tolls⁹, Steve Unwin¹, Tejaswi Venumadhav², Marco Viero⁴, Mike Werner¹, Mike Zemcov²

¹ *Jet Propulsion Laboratory, California Institute of Technology, Pasadena, CA 91109, USA*

² *California Institute of Technology, Pasadena, CA 91125, USA*

³ *IPAC, 1200 E. California Blvd., Pasadena, CA 91125, USA*

⁴ *Stanford University, Palo Alto, CA 94305, USA*

⁵ *Department of Physics & Astronomy, Johns Hopkins University, Baltimore, MD 21218, USA*

⁶ *Ohio State University, Columbus, OH 43210, USA*

⁷ *Korea Astronomy and Space Science Institute, Daejeon 305-348, Korea*

⁸ *Department of Physics and Astronomy, University of California, Irvine, CA 92697, USA*

⁹ *Harvard-Smithsonian Center for Astrophysics, Cambridge, MA 02138, USA*

¹⁰ *Argonne National Laboratory, Lemont, IL 60439, USA*

¹¹ *Institute for Astronomy, Hilo, HI 96720, USA*

¹² *Arizona State University, Tempe, AZ 85287, USA*

¹³ *Carnegie Mellon University, Pittsburgh, PA 15213, USA*

(Dated: March 27, 2015)

SPHEREx (Spectro-Photometer for the History of the Universe, Epoch of Reionization, and Ices Explorer) [Website] is a proposed all-sky spectroscopic survey satellite designed to address all three science goals in NASA's Astrophysics Division: probe the origin and destiny of our Universe; explore whether planets around other stars could harbor life; and explore the origin and evolution of galaxies. SPHEREx will scan a series of Linear Variable Filters systematically across the entire sky. The SPHEREx data set will contain $R=40$ spectra for $0.75 < \lambda < 4.1 \mu\text{m}$ and $R=150$ spectra for $4.1 < \lambda < 4.8 \mu\text{m}$ for every 6.2 arcsecond pixel over the entire-sky. In this paper, we detail the extra-galactic and cosmological studies SPHEREx will enable and present detailed systematic effect evaluations. We also outline the Ice and Galaxy Evolution Investigations.

I. SPHEREX MISSION OVERVIEW

SPHEREx (Spectro-Photometer for the History of the Universe, Epoch of Reionization, and Ices Explorer; PI: J. Bock) is a proposed all-sky survey satellite designed to address all three science goals in NASA's Astrophysics Division: probe the origin and destiny of our Universe; explore whether planets around other stars could harbor life; and explore the origin and evolution of galaxies. All of these exciting science themes are addressed by a single survey, with a single instrument, providing the first near-infrared spectroscopy of the complete sky. In this paper, we will focus on the cosmological science enabled by SPHEREx and outline the Galactic Ices and the Epoch of Reionization (EOR) scientific investigations.

SPHEREx will probe the origin of the Universe by constraining the physics of inflation, the superluminal expansion of the Universe that took place some 10^{-32} s after the Big Bang. SPHEREx will study its imprints in the three-dimensional large-scale distribution of matter by measuring galaxy redshifts over a large cosmological volume at low redshifts, complementing high-redshift surveys optimized to constrain dark energy.

SPHEREx will investigate the origin of water and biogenic molecules in all phases of planetary system formation - from molecular clouds to young stellar systems with protoplanetary disks - by measuring absorption spectra to determine the abundance and composition of ices toward $> 2 \times 10^4$ Galactic targets. Interstellar ices are the likely source for water and organic molecules, the chemical basis of life on Earth, and knowledge of their abundance is key to understanding the formation of young planetary systems as well as the prospects for life on other planets.

SPHEREx will chart the origin and history of galaxy formation through a deep survey mapping large-scale structure. This technique measures the total light produced by all galaxy populations, complementing studies based on deep galaxy counts, to trace the history of galactic light production from the present day to the first galaxies that ended the cosmic dark ages.

SPHEREx will be the first all-sky near-infrared spectral survey, creating a legacy archive of spectra ($0.75 \leq \lambda \leq 4.8 \mu\text{m}$ with $\lambda/\Delta\lambda = 41.5$, and a narrower filter width $\lambda/\Delta\lambda = 150$ in the range $\lambda = 4.12 - 4.83 \mu\text{m}$) with the

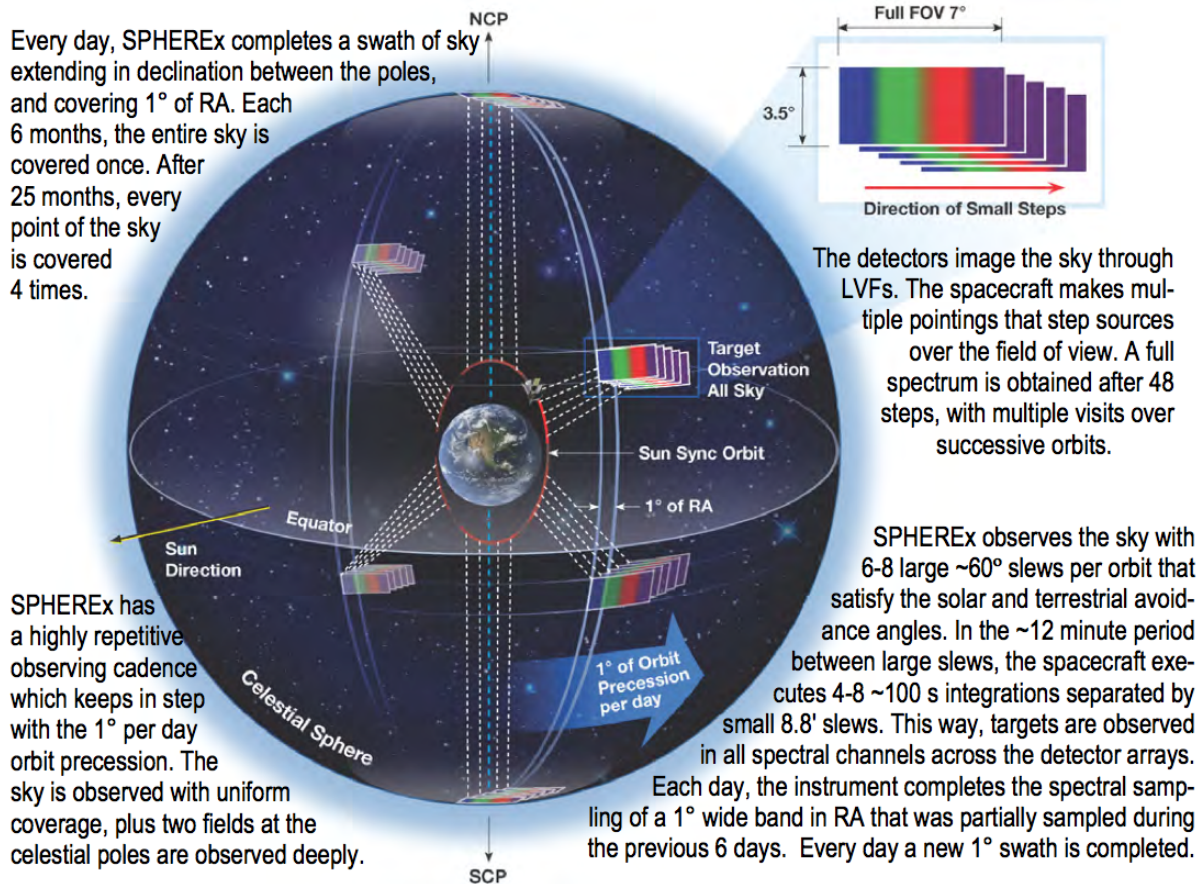


FIG. 1: SPHEREx completes an All-Sky map in a step and repeat fashion, one targeted observation at a time, separated by spacecraft slew maneuvers.

high sensitivity obtained using a cooled telescope with large spectral mapping speed. Space-borne measurements are essential, because the opacity of the Earth's atmosphere makes these observations functionally impossible across the relevant spectral range. The SPHEREx archive applies to numerous exciting and diverse astronomy investigations, some of which we can only imagine today. All-sky surveys such as the IRAS, COBE and WISE Explorer missions have played a major role in modern astrophysics, with a proven legacy that lasts for decades.

The SPHEREx Mission will implement an extremely simple and robust design that maximizes spectral throughput and efficiency. The instrument is based on a 20 cm all-aluminum telescope with a wide $3.5^\circ \times 7^\circ$ field of view, imaged onto four $2k \times 2k$ HgCdTe detector arrays arranged in pairs separated by a dichroic. These H2RG arrays have been fully qualified for space observations by JWST, and are built upon a long successful history of space instruments using arrays in smaller formats. Spectra are produced by four space-demonstrated linear-variable filters. The spectrum of each source is obtained by moving the telescope across the dispersion direction of the filter in a series of discrete steps (see Figure 1). This simple method was demonstrated by LEISA on New Horizons to obtain remarkable spectral images of Jupiter. Using thermal methods demonstrated by Planck, Spitzer and WISE, the telescope is radiatively cooled to ≤ 80 K and two of the detectors are cooled to ≤ 55 K with 450 % margin on the total heat load. SPHEREx has no moving parts except for one-time deployments of the sunshields and aperture cover.

SPHEREx will observe from a sun-synchronous terminator low-earth orbit, scanning repeatedly to cover the entire sky in a manner similar to IRAS, COBE and WISE. The feasibility study of such a sky strategy has been presented in [1]. During its two-year nominal mission, SPHEREx produces four complete all-sky spectral maps for constraining the physics of inflation. These same maps contain hundreds of thousands of high signal-to-noise absorption spectra to study water and biogenic ices. The orbit naturally covers two deep, highly redundant regions at the celestial poles, which we use to make a deep map, ideal for studying galaxy evolution. All aspects of the SPHEREx instrument and spacecraft have high heritage. SPHEREx requires no new technologies and carries large technical and resource margins on every aspect of the design. The projected instrument sensitivity, based on conservative performance estimates, carries 300 % margin on the driving point source sensitivity requirement.

In this paper, we present an overview of the all-sky survey focusing on its cosmological implications. We explain briefly the principle of our measurement in Sec. II and motivate it briefly in Sec. III before giving an overview of the galaxy redshift survey in Sec. IV. In Sec. V we describe our simulation pipeline before quantifying the cosmological implications in Sec. VII. In Sec. VIII we discuss potential systematics and the associated mitigation strategies enabled by SPHEREx. In Sec. X we illustrate briefly the legacy value of such a data-set, before detailing the scope of the SPHEREx Ice Investigation in Sec. XI and the Epoch of Reionization Investigation in Sec. XII.

II. SPECTROSCOPY WITHOUT A SPECTROMETER

SPHEREx performs its all-sky spectroscopic survey using a compact wide-field telescope with no moving parts that images the sky directly onto the focal plane through Linear Variable Filters (LVFs). Spectra are built up by stepping the instrument field across the sky with small motions of the spacecraft (see Figure 1).

SPHEREx is designed to maximize the spectral surveying power needed to map the entire sky (see Table I). In spite of its small aperture, SPHEREx achieves high spectral speed and overall power (see Figure 2) by the use of high-throughput, efficient optics coupled to large-format low-noise focal plane arrays. The instrument uses a small telescope that provides excellent image quality over a wide field, and LVFs that eliminate the reimaging optical elements and mass associated with conventional spectrometers.

LVFs specifically fabricated for the required wavelength range and resolving power, are mounted above the near-IR detector arrays – one for each array. Every column of pixels has a unique spectral response. Complete spectra are obtained by stepping these columns across the sky. The LVF wavelength ranges and resolving powers are chosen to allow a uniform step size survey while realizing higher spectral resolution in the longest wavelength band (see Figure 1).

III. SPHEREX ALL-SKY SURVEY MOTIVATION

The physics of inflation can be probed by measuring the imprint of inflationary ripples in the large-scale structure (LSS) distribution of galaxies (see Figure 3). Precise measurements of this distribution constrain the statistics of the inflationary ripples and provide a method for concrete discrimination between various models of the inflationary field(s) [2–4]. In particular, LSS of the low redshift Universe provides a powerful tracer of primordial non-Gaussianity, and therefore contains great potential to improve constraints on the physics of inflation [5, 6].

The design of the SPHEREx all-sky survey has been optimized to measure the large-scale distribution of galaxies, precisely quantifying the statistical distribution of the inflationary ripples. We can characterize the non-Gaussian departure in the distribution of the inflationary fluctuations from a Gaussian bell curve by the $f_{\text{NL}}^{\text{loc}}$ parameter [7, 8]. Inflation models fall into broad categories, and measuring $f_{\text{NL}}^{\text{loc}}$ provides a unique test. Inflation models driven by

Parameter	Value
Telescope Effective Aperture	20 cm
Pixel Size	6.2" × 6.2"
Field of View	2 × (3.5° × 7.0°); dichroic
Spectrometer Resolving Power and Wavelength Coverage	R=41.5; λ=0.75-4.1 μm R=150; λ=4.1-4.8 μm
Arrays	2 x Hawaii-2RG 2.5 μm 2 x Hawaii-2RG 5.3 μm
Point Source Sensitivity	18.5 AB mag (5σ) on average per frequency element with 300% margin
Cooling	All-Passive
2.5 μm Array and Optics Temperature	80K with 700% margin on total heat load
5.3 μm Array Temperature	55K with 450% margin on total heat load
Payload Mass	68.1 kg (current best estimate + 31% contingency)

TABLE I: SPHEREx Key Instrument Parameters.

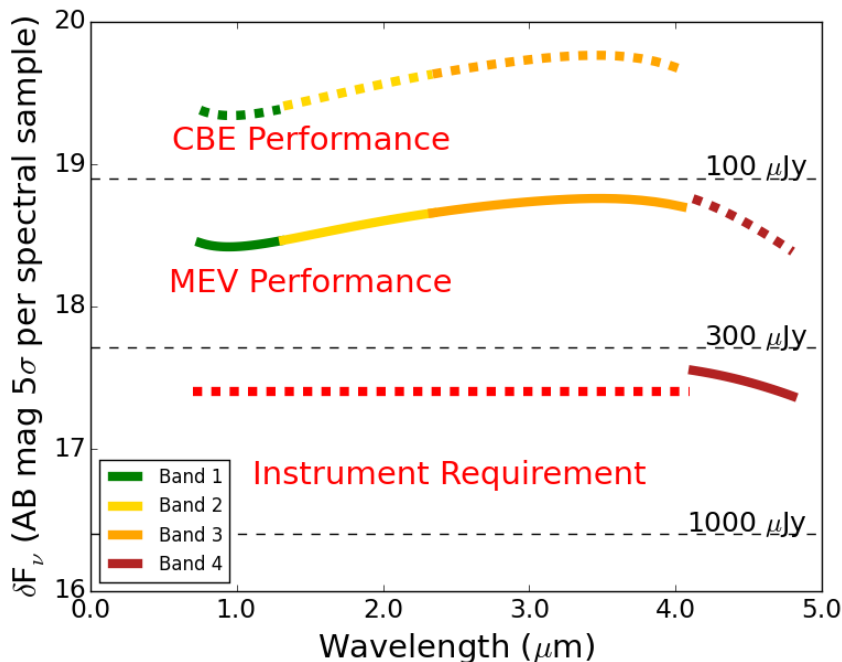


FIG. 2: SPHEREx scientifically required point source sensitivity has large margin over the estimated instrument performance. We show above the instrument requirement (red dashed line) and the MEV (solid colored curve) and CBE (dashed current curve) performance. The Maximum Expected Value (MEV) performance refers to the instrument performance based on specifications that each sub-system can meet with contingency. The Current Best Estimated (CBE) performance is the instrument performance based on currently estimated sub-system performance. The scientific margin is defined as the difference between MEV Performance and the Instrument Requirement. The Band 4 sensitivity easily meets the 12 AB mag (5) requirement, and will return hundreds of thousands of high-quality ice absorption spectra (see Sec. XI).

multiple fields generally predict a high-level of non-Gaussianity ($|f_{\text{NL}}^{\text{loc}}| > 1$) while simpler models with a single field generally predict low levels of non-Gaussianity ($|f_{\text{NL}}^{\text{loc}}| < 1$) [6].

The Planck satellite team has led a vigorous search for non-Gaussianity in the statistical properties of the CMB; however this approach is now near fundamental limits. Experimental advances in CMB technology produced a large improvement in $f_{\text{NL}}^{\text{loc}}$ measurements from WMAP to Planck [9, 10]. The most recent results constrain $f_{\text{NL}}^{\text{loc}}$ to be ≤ 14.3 (2σ), i.e., the energy fluctuations in the primordial Universe followed a Gaussian distribution to at least one part in 100,000. However, this constraint is not strong enough to rule out multi-field models. Unfortunately, the CMB is now largely exhausted for improving $f_{\text{NL}}^{\text{loc}}$ constraints. The ultimate CMB measurement, limited by fundamental cosmic variance, could only improve on the Planck errors by 60% [11].

Improved $f_{\text{NL}}^{\text{loc}}$ measurements thus require a new approach. Because an LSS survey maps the Universe in 3-D, it accesses many more modes than are available from the more limited 2-D CMB surface of last scattering. This allows LSS surveys to set much tighter constraints on $f_{\text{NL}}^{\text{loc}}$. SPHEREx will access the unprecedented large cosmic volume available and improve on Planck’s $f_{\text{NL}}^{\text{loc}}$ measurement by a factor of 10. It will achieve the sensitivity of $|f_{\text{NL}}^{\text{loc}}| < 1$ (2σ) required to distinguish between the single-field and multi-field scenarios.

IV. SPHEREX ALL-SKY GALAXY REDSHIFT OVERVIEW

SPHEREx measures 3-D LSS using a small telescope with an innovative spectroscopic capability, focusing on the low-redshift Universe to build a unique survey of unprecedented volume (see Figure 11). SPHEREx will determine redshifts for hundreds of millions galaxies from the all-sky catalog created from WISE [12], Pan-STARRS [13] and DES [14]. The redshift of these galaxies, pre-selected to avoid source blending, is obtained by fitting the measured spectra to a library of galaxy templates [15]. By observing at infrared wavelengths, SPHEREx leverages the well-known rest-frame $1.6 \mu\text{m}$ bump that is nearly universal in galaxy spectra and is a powerful redshift indicator (Figure 4, [16, 17]). Since Pan-STARRS and DES are substantially deeper than SPHEREx, using their galaxy catalog we can reliably estimate the confusion noise. Furthermore, using the above catalog, we will know before-hand these galaxies and will simply ignore the associated pixels when measuring the clustering of galaxies over the all-sky (both of these

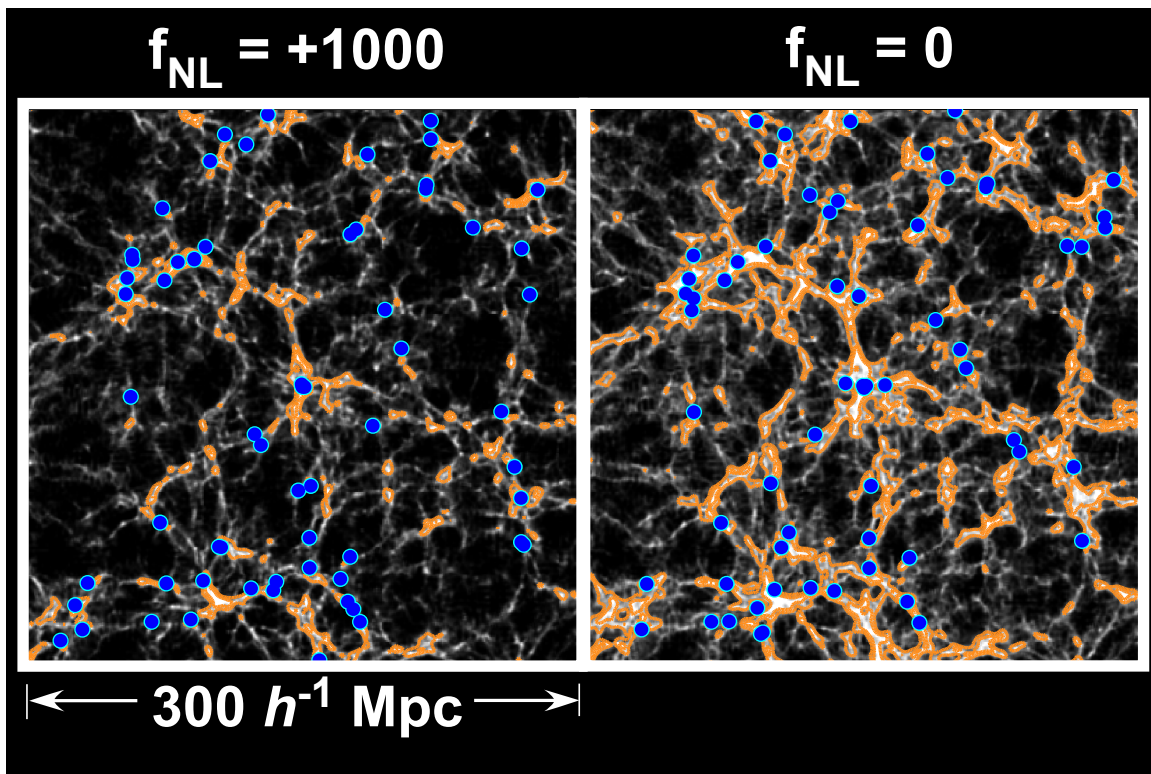


FIG. 3: By precisely measuring the spatial clustering of galaxies, SPHEREx will measure primordial non-Gaussianity described conveniently by the parameter $f_{\text{NL}}^{\text{loc}}$. This plot shows two simulated distributions of matter (color scales) and galaxies (blue dots) for different values of $f_{\text{NL}}^{\text{loc}}$. By precisely measuring the clustering of galaxies over a volume more than 10^5 times larger than depicted here, SPHEREx will measure $f_{\text{NL}}^{\text{loc}}$ to high accuracy.

effects are included in the simulations described before).

The template fit produces a galaxy type, an expected redshift, and a redshift uncertainty. We built a simulation and redshift fitting pipeline based on the tools used to produce the official photometric forecasts for the Euclid and WFIRST missions [18] including realistic source confusion, clustering, colors, and both random and systematic photometric errors. The power of low-resolution ($R \simeq 20-100$) spectra such as those obtained by SPHEREx for cosmological studies has been successfully demonstrated by the ground-based PRIMUS [19], COSMOS [15], and NMBS [20] surveys, and our pipeline reproduces the observed redshift accuracy in these surveys (it also motivates planned survey such as J-PASS and PAU [21, 22]). The redshift error is strongly dependent on the brightness of the galaxy – brighter galaxies produce smaller errors. Therefore, we classify galaxies according to their redshift accuracy, obtaining $\simeq 300$ million with accuracy $\sigma(z)/(1+z) \leq 10\%$ and $\simeq 9$ million with 0.3% accuracy. As shown in Figure 10 the distribution of galaxies extends out to moderate redshifts, covering a very large effective volume (Figure 11).

V. SPHEREX FULL-SKY SURVEY SIMULATION PIPELINE

In this section, we present an overview of our data-analysis/simulation pipeline. While most of it follows standard procedure in the era of CCD astronomy, we emphasize some SPHEREx peculiarities.

A. Overview

An overview of our pipeline is described in the flow diagram depicted in Figure 5. It highlights the interplay between pre-flight, on-board and ground processing. It also shows the role of external full-sky catalogs we will rely on for the astrometry, the photometric calibration and the optimal photometry solution. We describe each of these steps in the coming sub-sections.

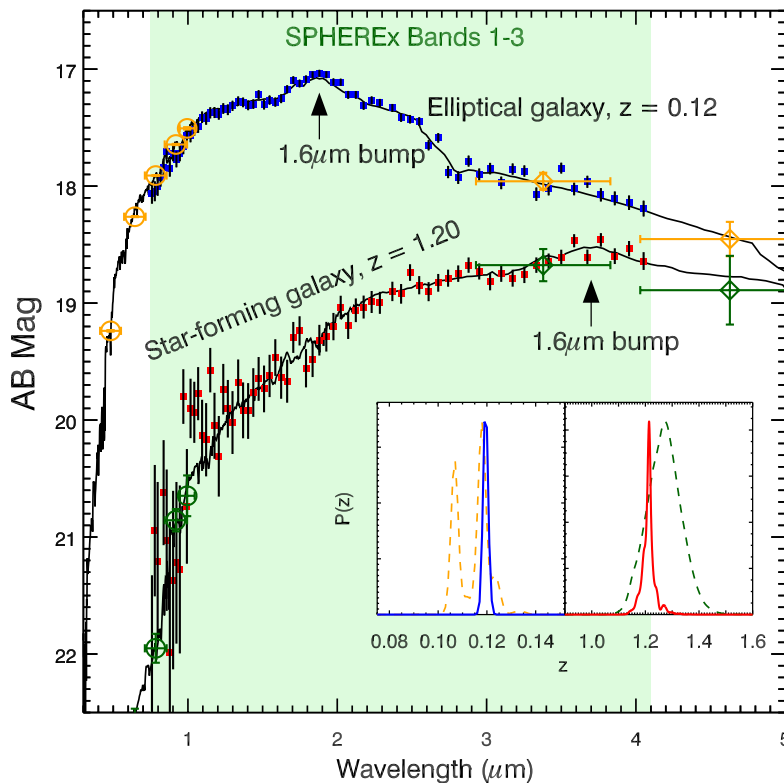


FIG. 4: SPHEREx determines the redshifts of WISE (diamonds) and Pan-STARRS/DES (circles) galaxies by fitting their measured spectra. Each redshift is assigned an error, a process we have extensively simulated from the COSMOS galaxy catalog. The determination is strongly driven by the $1.6 \mu\text{m}$ bump, so the target redshift range is well-matched to the $0.75 \leq \lambda \leq 4.1 \mu\text{m}$ wavelength coverage. We require a minimum redshift error $\Delta z/(1+z) = 0.5\%$ to access the finest useful physical scales, which requires a spectral resolution of 35.

B. Reduction and calibration

The first step of the low level data analysis is to read raw telemetered data and produce calibrated, flat-fielded and astrometrically aligned images for each individual exposure. The data reduction pipeline to final maps is outlined in Figure 5, and we summarize the essential elements below. The accuracy to which we estimate controlling the various contributions of systematic error of each step in the pipeline will be discussed later in section VIII.

- Raw Telemetered Data to Sky Images:** The SPHEREx focal planes are populated with a total of four H2RG HgCdTe charge integrating detectors, manufactured by Teledyne systems. They are imaged to the sky with an instantaneous FOV of $3.52^\circ \times 3.52^\circ$ sampled by 6.2 arcsecond pixels. Due to bandwidth constraints, the raw $2048 \times 2048 \times 4$ array frames sampled at $1.5 \sim \text{s}$ intervals can not be telemetered directly to Earth. Instead, we will implement on-board software to fit lines to the charge integration for each pixel to produce photocurrent images of each exposure. The slope fit images in units of e^-/s are then downlinked to Earth. A series of binary flags which identify events such as cosmic rays, saturation and non-linearity accompany the images. The final data product returned for each exposure is a sub-sample of 8×32 pixels at the full frame rate used to monitor the noise and verify the on-board software is performing adequately.
- Dark Current Correction.** The detectors have a zero-signal response termed dark current (DC), for H2RGs, the mean value is typically $\sim 0.01 e^-/\text{s}$. A DC template for the specific arrays will be constructed from extensive laboratory characterization prior to launch and will be subtracted from each image at the first level of ground based processing. Additionally, sections of each array will be masked in flight to monitor drifts in the DC throughout the mission.
- Flat Fielding.** Due to inhomogeneities in fabrication, each pixel has a unique responsivity to incoming photons. A measurement of the instrument's response to a spatially flat input illumination (a flat field) is used to correct the sky images for these variations. We will estimate the flat field response both from laboratory measurements

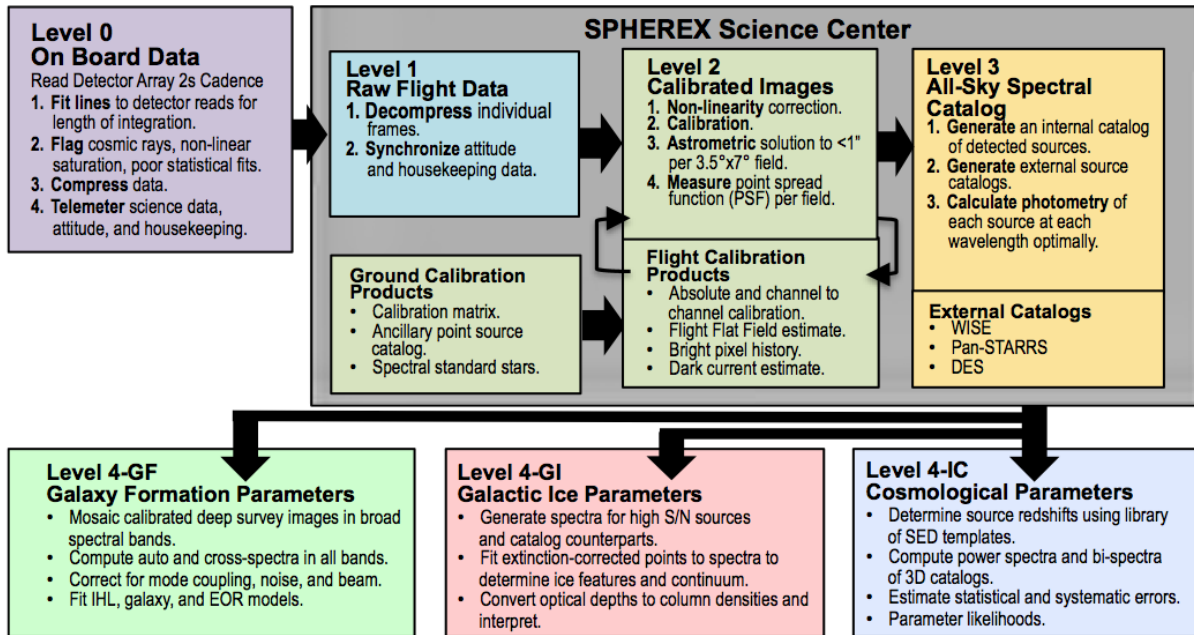


FIG. 5: Overview of the planned SPHEREx analysis pipeline, going from raw telemetered data to calibrated multi-wavelength images and various science studies.

using a field-filling, uniform radiance source with a solar-like spectrum before launch, as well as the diffuse sky brightness itself in flight. The redundant and dithered scan strategy at the celestial poles offer an excellent dataset to apply this self calibration technique.

- **Astrometric Registration.** Generation of the absolute pointing solution for each field will begin with the spacecraft attitude information, accurate to 15 arcseconds. We will then apply a demonstrated astrometry identifying algorithm Lang et al. [23] to the SPHEREx data itself, referenced to a USNO-B +2MASS stellar catalog, producing a solution accurate to the sub-arcsecond level.
- **Point Spread Function Generation.** Flux extraction of unresolved sources using optimal photometry requires an accurate understanding of the PSF. For each wavelength in each exposure, we will generate a PSF template by stacking all stellar sources in the 2MASS catalog. Each spatial/spectral sample in SPHEREx spans a solid angle of 0.53 deg^2 , for moderately high Galactic latitude fields, this will contain 350 stars with J-band magnitudes brighter than 14th.
- **Flux Calibration.** SPHEREx will rely on a combination of laboratory measurements and in-flight characterization for absolute flux calibration. In the laboratory, injecting a broad-band light source into a uniformly illuminating integrating sphere monitored by NIST-calibrated reference photodetectors has been demonstrated to produce percent level accuracy of absolute calibration [24–26]. Additionally, as SPHEREx is an all sky survey, we will observe all of the 97 spectral standard stars available from the STSCI database. The resulting calibration factors will be applied to the data at this stage.

After the aforementioned processing, the data for each exposure will consist of 4 calibrated images with wavelength varying across the FOV. These will be used as the input to the source flux extraction described below.

VI. BUILDING A GALAXY CATALOG

In this section, we describe how we go from a collection of calibrated images at multiple wavelengths to a galaxy catalog characterized by its position and its redshift. We outline the method we employ, demonstrated using a state of the art simulation pipeline. In particular, this section describes the path from calibrated images to the galaxy catalog as outlined in the top half of Figure 6.

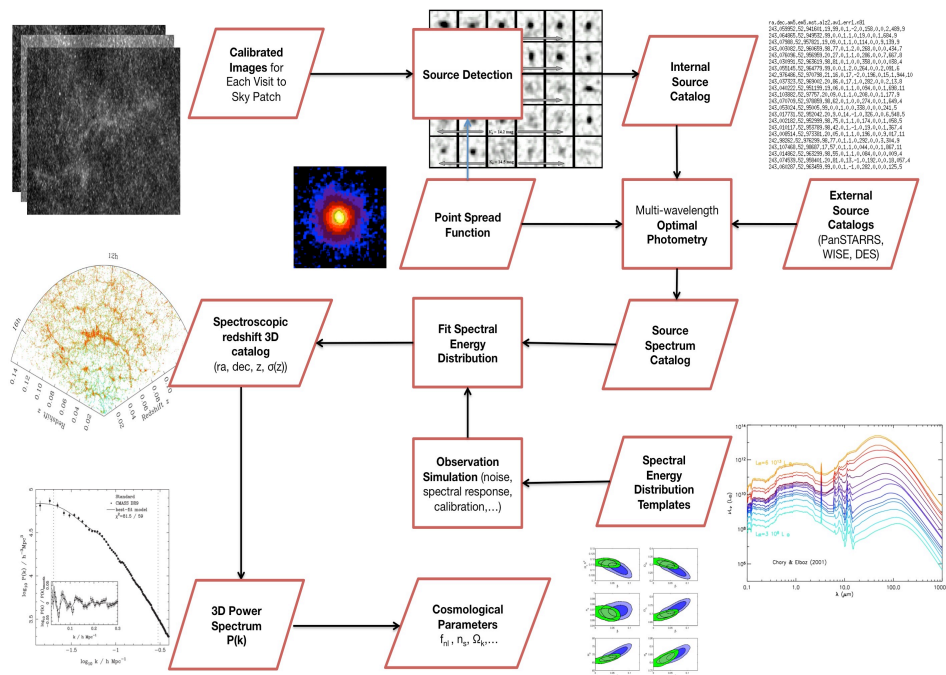


FIG. 6: Flow diagram illustrating the process to go from calibrated multi-wavelength images to cosmological constraints.

A. Simulation pipeline principles

We use real galaxy data from the Cosmic Evolution Survey (COSMOS, Scoville et al. 2007) to create realistic simulated SPHEREx observations. Extracted photometry from objects in these simulated observations is passed to a high-performance redshift template-fitting code. The quality of the derived redshifts is then analyzed in detail to understand the ability of SPHEREx to constrain cosmological parameters. Our goal with the simulation pipeline is to produce the most realistic forecast possible, based on our empirical knowledge of the galaxy population. We note that this pipeline is used jointly by Capak et al. to produce official forecasts for the Euclid consortium, the WFIRST SDT as well as the Hyper-Suprime-Cam (HSC) Subaru survey.

B. Simulation pipeline overview

There are five main steps to the SPHEREx simulation pipeline:

1. Create the input galaxy catalog based on real data from the multi-wavelength COSMOS survey.
2. Generate simulated SPHEREx images at each wavelength step of the LVF based on the simulated galaxy spectral energy distributions (SEDs).
3. Optimally extract the $R \sim 40$ photometry from the simulated SPHEREx images.
4. Derive the photometric redshifts for all detected objects using a highly-optimized template fitting code based on *Le Phare* (Arnout & Ilbert 2011).
5. Compare the derived photo- z 's with the input galaxy catalog to test for redshift quality and derive the galaxy number counts $N(z)$ at different levels of redshift precision.

In the following sections we describe these steps in more detail.

C. Generating the Input Galaxy Catalog

The COSMOS survey comprises broad, medium, and narrow-band imaging over 2 deg^2 in 30 photometric bands spanning the near-UV to the infrared. Extensive SED fitting analysis has been done on galaxies in the COSMOS field,

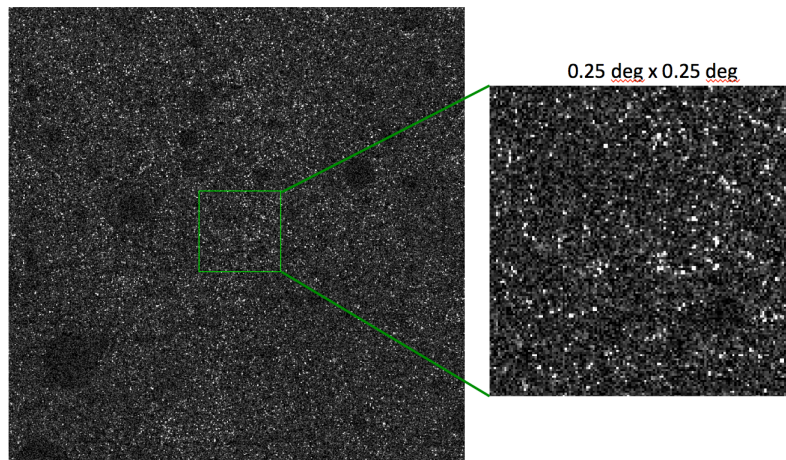


FIG. 7: Simulated data from SPHEREx in a spectral element of width $\Delta\lambda/\lambda=40$ centered at 1.93μ on the COSMOS field.

resulting in estimates for each source of (1) photometric redshift, (2) SED type (from the 31 galaxy templates used by Ilbert et al. 2009), (3) selective dust attenuation $E(B-V)$, and (4) reddening law. Together with the magnitudes of the objects, these parameters let us generate realistic models of the SEDs of the COSMOS sources over the entire wavelength range spanned by the SPHEREx observations. The input catalog thus consists of a set of known galaxy coordinates, magnitudes, redshifts, and SEDs. Because the simulated galaxies are based on real observations, they closely resemble the actual distribution of galaxies both in physical coordinates and parameter space.

D. SPHEREx Image Simulation

We assume a single set of LVF filters matching the design specifications. For each wavelength step in the LVF, the predicted flux of each object is computed by integrating its modeled SED against the filter profile at that wavelength. This flux is then added to a simulated image oversampled by a factor of 8 relative to the SPHEREx detector (i.e., to a grid with pixel scale $6''/2/8$). This is repeated for all simulated objects. Once the fluxes of all simulated objects have been added to the oversampled images, the images are smoothed with a Gaussian with FWHM $1.22\lambda/D$ to represent the SPHEREx PSF at a given wavelength. Another Gaussian smoothing is performed to take into account the effect of geometric aberrations that dominate over diffraction (by design) over much of the wavelength coverage. A last Gaussian smoothing is performed to simulate the effect of pointing smear. Finally the images are rebinned to the SPHEREx pixel size of $6''/2$ and Gaussian noise is added to reflect the depth of the SPHEREx observations. Because the simulated images are based on real galaxies and include sources far below the SPHEREx sensitivity, the effects of source confusion and noise due to faint objects are realistically captured in the simulated images.

In addition to the simulated SPHEREx images, we use the modeled COSMOS galaxy SEDs to generate simulated Pan-STARRS [13] ground-based photometry in *ugriz* and WISE photometry in the $3.4\mu\text{m}$ (W1) and $4.6\mu\text{m}$ (W2) bands [12]. Appropriate noise is added to these simulated observations, which represent ancillary data that will be available to the SPHEREx mission.

E. Source extraction

The large instantaneous field-of-view required for a survey such as SPHEREx, combined with the constraints placed by maintaining a reasonable total number of detectors, led to the optimized design plate scale of $6''/2/\text{pixel}$. The point spread functions of SPHEREx will have a range of full width at half maxima (FWHM) of $5'' - 7''$ depending on the wavelength. This combination of parameters results in an under-sampled PSF, in which the relative alignment of a point source on the sky and the coarse SPHEREx detector grid alters the shape of the observed PSF.

For an unresolved source in a survey with a well known PSF P , the optimal photometric extraction of the total flux F is obtained by the weighted sum

$$F = \sum_{i,j} w_{i,j} D_{i,j}, \quad (1)$$

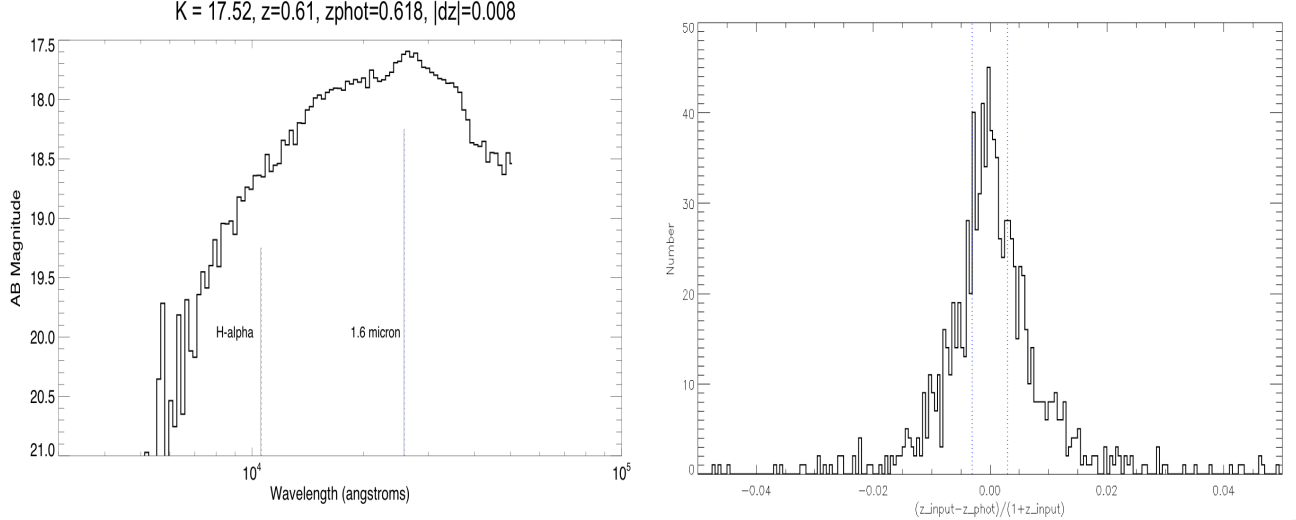


FIG. 8: Left :Example extracted SED for a bright object in the SPHEREx simulation pipeline. Right: The actual error distributions of objects with $\sigma(z)/(1+z) \leq 0.003$. The errors are computed as described in Sec. VI G.

where $D_{i,j}$ is the sky-subtracted flux measured in pixel (i, j) and the weight function w is constructed as

$$w_{i,j} = \frac{P_{i,j}}{\sum_{i,j} P_{i,j}^2}. \quad (2)$$

Here $P_{i,j}$ is the fraction of the PSF falling in pixel (i, j) . In the all-sky survey proposed for SPHEREx, the noise budget is dominated by photon noise from zodiacal light, which is diffuse and nearly uniform across the FOV. To quantify the signal-to-noise of a given detection and how it varies with the relative alignment of the detector grid, it is useful to define the parameter

$$N_{eff} = \sum_{i,j} \frac{1}{P_{i,j}^2}, \quad (3)$$

which represents the effective number of pixels spanned by the PSF. As N_{eff} increases, the signal from the source is spread over more pixels and the noise increases by the square root of the number of pixels. Therefore, in optimal photometry, the uncertainty in recovered source flux is related to N_{eff} by

$$\delta F = \sqrt{N_{eff}} [\delta F(1)] \quad (4)$$

where $\delta F(1)$ is the uncertainty in flux achieved for a PSF which is a perfect single pixel square step function.

For SPHEREx, N_{eff} will increase systematically with wavelength because of the growth of the diffraction limited PSF. Additionally, for a single wavelength, there is a significant spread in N_{eff} caused by the random alignment of sources with the detector grid. If a source falls closer to the corner of a pixel, its flux will spill over to neighboring pixels, while a source landing in the center will deposit most of its energy in a single pixel. Figure 9 shows the expected range of N_{eff} as a function of wavelength.

We extract sources in the simulated SPHEREx images optimally, with the true position of the objects on the detector known from the higher-resolution ground-based Pan-STARRS/DES data. This is close to how extraction will be performed in practice. With the position of the object known, the absolute pointing reconstructed to $< 1''$, and the PSF accurately characterized in every image, the values of $P_{i,j}$ that go into the weight function for optimal extraction can be computed. To do this, the normalized PSF is resampled onto a fine grid centered at the known position of the object on the detector, and the value of $P_{i,j}$ in the nearby pixels is found by summing the portion of P falling within pixel (i, j) . In general, the optimally extracted object fluxes match the input fluxes well.

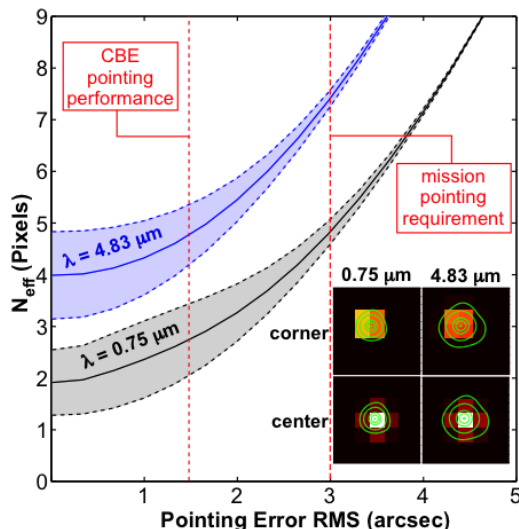


FIG. 9: SPHEREx measures the flux of known sources by combining pixels with optimal weights. The effective number of pixels, $N_{eff} = 1/\sum p_j^2$ affects the flux sensitivity as $N_{eff}^{1/2}$, where p_j is the PSF of the j^{th} pixel. The plot shows N_{eff} at two wavelengths, calculated from the optical PSF with geometric and diffractive PSFs combined with optical tolerance errors, as a function of system pointing. N_{eff} depends on source position relative to pixel edges (shaded range).

F. Redshift Determination

Once the fluxes of the objects have been extracted from the simulated SPHEREx images, we compute redshift estimates by fitting template SEDs to the observations. Because of the large number of filters and the high degree of precision with which we wish to measure the redshift, off-the-shelf photo-z codes cannot be used. Instead, we developed a version of the *Le Phare* code written in highly optimized C. As with *Le Phare*, template fitting against the 31 basis SEDs from COSMOS is performed against each extracted object to determine the redshift probability density function (PDF) $P(z)$. For each model SED, we sample redshift from 0-2 in steps $dz = 0.0005$, E(B-V) values from 0-1 in steps of $dE(B-V)=0.05$, and four reddening laws, for 10,418,604 total model grid points. The expected flux in the SPHEREx bands of each model in the grid is pre-computed by integrating the modeled SED against the LVF filter profiles and stored in a file prior to the template fitting.

The fitting of the photometry from the observed SPHEREx objects to the model grid is parallelized for efficiency. For each object, the χ^2 offset between the object's photometry and each point in the model grid is computed after normalizing the model to the observed photometry. The value of $P(z)$ at each redshift step is computed by summing the likelihood $e^{-\chi^2/2}$ of all models (SED, E(B-V), reddening law) at that redshift step, thus marginalizing out those parameters. In this way we derive finely sample $P(z)$ estimates for the simulated SPHEREx sources.

G. Error characterization

From the likelihood function $P(z)$ we find the best redshift estimate \bar{z} for each object through the expectation value,

$$\bar{z} = \frac{\sum_i z_i P(z_i)}{\sum_i P(z_i)}, \quad (5)$$

where i runs over all redshift steps. The error in this estimate is extracted from the PDF through

$$\sigma_{\bar{z}} = \sqrt{\frac{\sum_i (z_i - \bar{z})^2 P(z_i)}{\sum_i P(z_i)}}. \quad (6)$$

These estimates can then be compared with the known input redshifts to test the performance.

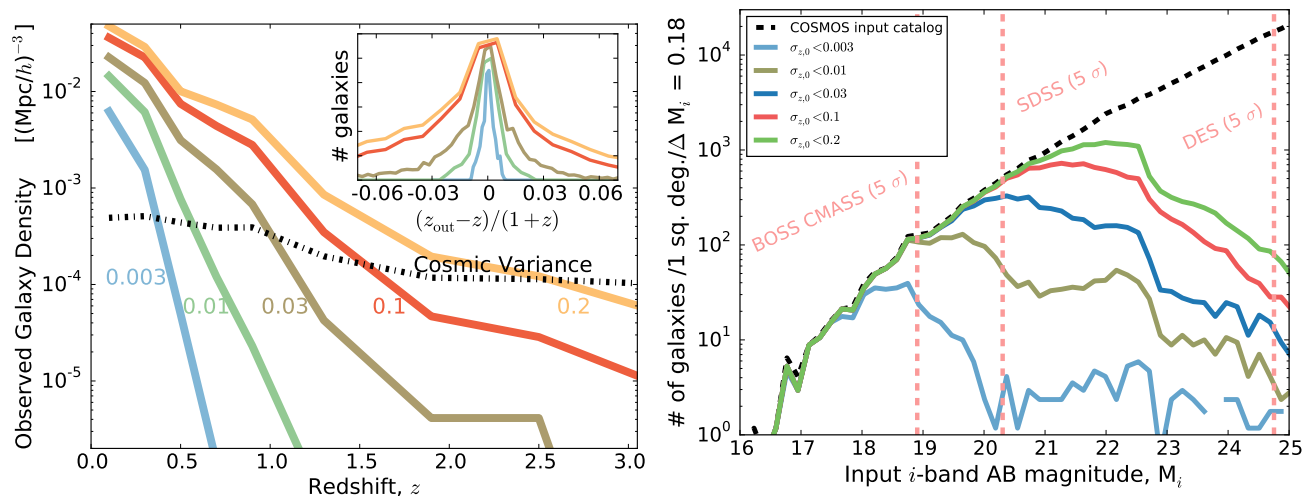


FIG. 10: Left: SPHEREx measures the redshifts of over 500 million galaxies, an unprecedented dataset. Accuracy bins are labeled by their maximum $\tilde{\sigma}_z \equiv \sigma(z)/(1+z)$. The large sample of low-accuracy (0.1) redshifts constrains $f_{\text{NL}}^{\text{loc}}$ in the power spectrum. The sample of high-accuracy (0.003) redshifts allows clustering measurements on smaller scales and constrains power spectrum parameters and the bispectrum. The low-accuracy sample ($\tilde{\sigma}_z < 0.1$) achieves the cosmic variance limit (black dashed curve) out to redshift $z = 1.6$. The unnormalized histograms of the simulated redshift errors are shown in the inset. Right: Illustration of the i -band magnitude distribution of SPHEREx galaxies as a function of redshift accuracy. The dashed black line shows the distribution of the input COSMOS catalog. Also shown are approximate completeness limits for existing surveys (vertical dashed lines).

H. Final catalogs and characteristics

Applying the previous pipeline to our synthetic data-set leads to a 3-D galaxy catalog with well characterized properties. As we will discuss below it is beneficial to separate the catalog into multiple populations with different measured redshift accuracies as they will correspond to galaxy populations with different bias, and will thus lead to the potent use of multi-tracer techniques proposed in McDonald and Seljak [27] and demonstrated observationally with the GAMA survey [28]. Besides, different cosmological parameters, for example $f_{\text{NL}}^{\text{loc}}$ or α_s have different redshift accuracy requirements. In Figure 10 we illustrate the reconstructed comoving number density of our sample for various redshift accuracy bins and the associated i -band AB magnitude distribution. In Figure 11 we combine this comoving densities with SPHEREx all-sky capabilities to compute the survey effective volume and compare it to other current or planned cosmological surveys. We note that for SPHEREx we use only 75% of the sky to account for the required galaxy masking. Similarly, bright regions will be masked when performing the cosmological analysis in an analogous manner to what is performed e.g., for the WMAP or Planck analysis.

VII. COSMOLOGICAL FORECASTS

In this section we introduce the methodology used to forecast the cosmological constraints obtainable with the SPHEREx galaxy catalog.

A. General Methodology

We will rely on the Fisher matrix formalism (see, e.g., [29]). As an input, we will consider the galaxy catalog produced with the simulation pipeline described above. We divide the output catalog into N_z redshift bins with bounds $\{z_i^{\text{min}}, z_i^{\text{max}}\}_{i=1}^{N_z}$. We use a large number of redshift bins and have tested that we are in the regime where the forecasted constraints have become insensitive to the exact binning. We subsequently divide the galaxy catalogs into N_{σ_z} redshift accuracy bins with bounds $\{\tilde{\sigma}_{z,j}^{\text{min}}, \tilde{\sigma}_{z,j}^{\text{max}}\}_{j=1}^{N_{\sigma_z}}$, where $\tilde{\sigma}_z \equiv \sigma_z/(1+z)$ and σ_z the estimated redshift uncertainty of a galaxy. Ultimately, our input catalog leads to a collection of mean densities $\bar{n}_j^g(z_i)$. For each redshift bin z_i , the forecasts rely on not only the number densities of the subsamples, but also the values of their mean redshift scatter, $(1+z_i)\tilde{\sigma}_{z,j}$, and of their galaxy bias, $b_j(k, z_i)$. The former is estimated directly from the catalog by computing

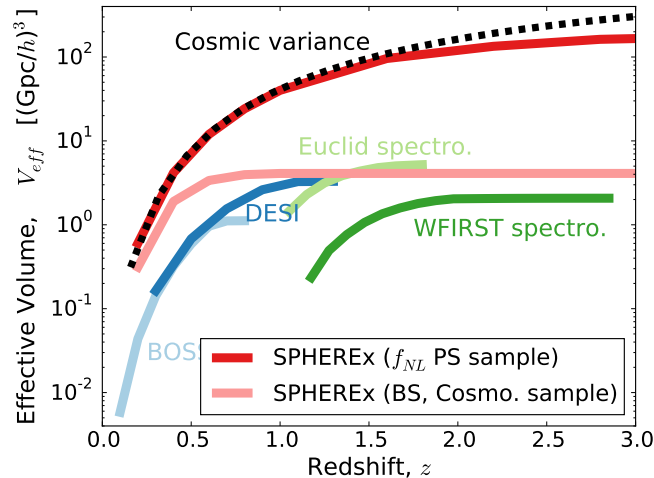


FIG. 11: Effective volume mapped by SPHEREx. The effective volume is the physical volume mapped by a given survey, corrected for the sampling noise of a finite number of galaxies ($V_{eff}(z) = V_{survey}(z) \sqrt{P_{gg}(k_0, z)/(P_{gg}(k_0, z) + 1/\bar{n})}$). For a well-sampled survey, the effective volume equals the physical volume. The cosmological information content of a given survey is directly proportional to the number of independent spatial modes, and directly proportional to the effective volume. The SPHEREx f_{NL}^{loc} power spectrum (PS) sample (red curve) extracts all the cosmological information up to $z \simeq 1.5$ (black dashed curve). The SPHEREx bispectrum (BS) and cosmological parameters sample (pink curve), based on a smaller sample of high redshift accuracy galaxies, is uniquely powerful at $z < 1$ compared with other planned surveys. The effective volume is calculated based on the galaxy power spectrum at $k_0 = 0.001h/\text{Mpc}$, which is approximately the scale that delivers most of the information on f_{NL}^{loc} .

the scatter in $(\hat{z} - z)/(1 + z)$ (where \hat{z} is the redshift estimate in the catalog, and z is the true/input redshift) of all galaxies in the j -th $\tilde{\sigma}_z$ -bin, and generally the resulting $\tilde{\sigma}_{z,j}$ lies somewhere in between the defining bounds, $\tilde{\sigma}_{z,j}^{\min} - \tilde{\sigma}_{z,j}^{\max}$. The galaxy bias is estimated using abundance matching, as described in more detail in section VII B. Dividing the sample into different $\tilde{\sigma}_z$ -bins ensures that we have subsamples with different galaxy bias, which enables us to use the multi-tracer technique to optimize cosmological constraints, especially those on primordial non-Gaussianity [30–32].

Once the above ingredients, i.e., number density, redshift scatter and galaxy bias for each redshift and redshift uncertainty bin, are computed, we use standard Fisher matrix forecasting methods to calculate expected parameter constraints from the galaxy power spectrum (Section VII C) and bispectrum (Section VII D). While the effects of cosmological parameters on large-scale structure and the expansion history of the universe are well known, we wish to highlight the effect of the local primordial non-Gaussianity parameter, f_{NL}^{loc} , as this parameter will be particularly well constrained by SPHEREx. In the presence of primordial non-Gaussianity, the linear halo bias receives a scale-dependent correction [4, 33–35],

$$b_j(k, z) = b_{G,j}(z) + 2 f_{NL}^{loc} (b_{G,j}(z) - 1) \delta_c \frac{3\Omega_m H_0^2}{2k^2 T(k) D(z)}. \quad (7)$$

Here $b_{G,j}(z)$ is the Eulerian, Gaussian halo bias in the j -th subsample at redshift z , and δ_c is the critical overdensity for halo collapse, here taken to be the critical density for spherical collapse, $\delta_c = 1.686$. Furthermore, Ω_m is the matter density at $z = 0$ relative to the critical density, H_0 the Hubble constant ($z = 0$), $T(k)$ is the transfer function of matter perturbations, normalized to 1 at low k , and $D(z)$ is the linear growth function, normalized such that $D(z) = 1/(1 + z)$ during matter domination. A key feature of this bias correction that will be important later is that the effect is proportional to $k^{-2}/T(k)$ and therefore most important on large scales. The bias correction is of order f_{NL}^{loc} at the horizon scale. Moreover, the bias correction is proportional to $b_G - 1$, so that there is no scale dependence for an unbiased tracer.

B. Galaxy bias prescription

The Gaussian galaxy bias $b_{G,j}(z)$ (i.e., the bias in the absence of primordial non-Gaussianity) is a crucial input to the Fisher forecasts, with large bias generally being very beneficial for f_{NL}^{loc} studies. The catalog directly gives us the mean value of $\tilde{\sigma}_z$ for each redshift accuracy subsample and the number density as a function of redshift.

We obtain an estimate of the galaxy bias for each subsample (and each redshift bin) using the abundance matching technique. Specifically, at each redshift, we match the galaxies with the lowest redshift uncertainty to the host halos with the largest total mass. In practice, at a redshift z , we first find the minimum halo mass $M_{h,\min}$ of the j -th redshift accuracy subsample by equating

$$\bar{n}_h(M_h > M_{h,\min}; z) = f_{\text{cen}} \bar{n}^g(\tilde{\sigma}_z < \tilde{\sigma}_{z,j}^{\text{max}}; z). \quad (8)$$

The central galaxy fraction factor, f_{cen} , accounts for the fact that if satellite galaxies were included, there would not be a one-on-one mapping between galaxies and halos. We take its value to be $f_{\text{sat}} = 0.8$, consistent with recent halo occupation distribution studies (e.g., [36]). For the halo number density, \bar{n}_h , we use the halo mass function fitting formula from [37]. Specifically, we use their universal mass function, calibrated on N-body simulations, and apply the empirical redshift scaling $(1+z)^{-0.26}$. The value of \bar{n}^g is obtained directly from the catalog. Once $M_{h,\min}$ is found, we simply set the galaxy bias to the halo bias of halos with mass $M_{h,\min}$,

$$b_{G,j}(z) = b_h(M_{h,\min}; z). \quad (9)$$

The halo bias on the right hand side above is computed from the fitting formula provided in [38], which is based on N-body simulations.

Our method is crude, but gives a reasonable enough estimate of the galaxy bias for the sake of our Fisher forecasts. The abundance matching assumption is likely violated to some extent, which would lower the bias. In this sense, our approach is optimistic, as large bias is beneficial for (especially) $f_{\text{NL}}^{\text{loc}}$. On the other hand, we are making a conservative choice by using the halo bias *at* the halo mass $M_{h,\min}$ matched to galaxies at $\tilde{\sigma}_{z,j}^{\text{max}}$, i.e., to the galaxy in the subsample with the largest redshift scatter and, accordingly, the lowest halo mass and halo bias in the abundance matching picture. In this sense, our approach is conservative.

C. Power spectrum forecasts

For the power spectrum forecast, we to a large extent follow [39, 40]. We use the information in the full shape of the three-dimensional, redshift-space, galaxy power spectrum $P_g(k, \mu)$, where k is the wave vector of a galaxy overdensity mode in Fourier space, and μ is the cosine of the angle between the mode and the line-of-sight direction (we assume the plane-parallel approximation throughout). Since we restrict our analysis to linear and mildly non-linear scales, the starting point for our power spectrum description is the linear Kaiser model [41]. For a given subsample,

$$P_{g,j}(k, \mu; z) = b_j^2(k, z) \left[1 + \frac{f(z)}{b_j(k, z)} \mu^2 \right]^2 P_m^L(k; z). \quad (10)$$

Note that $b_j(k, z)$ is related to the Gaussian bias $b_{G,j}(z)$ by Eq. (7). In the above, f is the linear growth rate of matter perturbations, which enters through redshift space distortions, and P_m^L is the linear matter power spectrum.

The power spectrum estimated from data is based on the three-dimensional coordinates of galaxies, which are obtained from the observed angular positions and redshifts by assuming a reference cosmology. If there is a mismatch between the reference cosmology and the true one, the scales appearing in the estimated power spectrum will be off from the truth. Specifically, wave vectors in the reference cosmology are related to the true wave vectors by

$$k_{\perp,\text{ref}} = \frac{D_A(z)}{D_{A,\text{ref}}(z)} k_{\perp}, \quad k_{\parallel,\text{ref}} = \frac{H_{\text{ref}}(z)}{H(z)} k_{\parallel}, \quad (11)$$

where $D_A(z)$ is the angular diameter distance, and $H(z)$ the Hubble parameter. Moreover, the change in volume due to using the reference cosmology causes a vertical shift in the estimated power spectrum. The effects described above encode the geometrical information in the galaxy clustering measurement, including information from the BAO scale and the Alcock-Paczynski effect. We therefore take these geometric shifts into account in our model for the observed galaxy power spectrum.

Another effect that needs to be included is that, when a sample of galaxies has non-negligible redshift scatter, $\sigma_z = (1+z)\tilde{\sigma}_{z,j}$, this causes a suppression of the observed power spectrum in the radial direction (see e.g., [42]). Putting it all together (except for a non-linear correction that we will add at the level of the Fisher matrix itself), we end up with the following model for the observed galaxy power spectrum (after shot noise subtraction),

$$P_{g,j}(k_{\perp,\text{ref}}, k_{\parallel,\text{ref}}; z) = e^{-((1+z)\tilde{\sigma}_{z,j})^2 / H_{\text{ref}}^2(z) k_{\parallel,\text{ref}}^2} \frac{D_{A,\text{ref}}(z)^2 H(z)}{H_{\text{ref}}(z) D_A(z)^2} b_j^2(z) \left[1 + \frac{f(z)}{b_j(k, z)} \frac{k_{\parallel}^2}{k^2} \right]^2 P_m^L(k; z), \quad (12)$$

where the physical wave vectors k_{\parallel}, k , etc. are related to the wave vectors in the reference cosmology by Eq. (11).

Finally, we implement a prescription for the damping of the power spectrum and smearing of the BAO feature due to the non-linear effect of bulk flows (e.g., [39]). The damping factor in the power spectrum is

$$\exp \left[-\frac{1}{2} k^2 \Sigma_{\perp}^2 - \frac{1}{2} k^2 \mu^2 (\Sigma_{\parallel}^2 - \Sigma_{\perp}^2) \right], \quad (13)$$

where the Lagrangian displacement fields Σ_{\parallel} and Σ to model the smearing effect are given as

$$\Sigma_{\perp}(z) \equiv c_{\text{rec}} D(z) \Sigma_0, \quad (14)$$

$$\Sigma_{\parallel}(z) \equiv c_{\text{rec}} D(z) (1 + f(z)) \Sigma_0, \quad (15)$$

with $D(z)$ the linear growth normalized to unity at $z = 0$. The present-day Lagrangian displacement field is $\Sigma_0 = 11h^{-1}\text{Mpc}$ for $\sigma_8 = 0.8$ [43]. The parameter c_{rec} , which we set to $c_{\text{rec}} = 0.5$, models the effectiveness of the reconstruction method of the BAO peak [43, 44]. We take the exponential factor of the smearing effect outside of the derivatives of the galaxy power spectrum in the Fisher matrix (see below). This is equivalent to marginalizing over uncertainties in Σ_{\parallel} and Σ_{\perp} .

In the above, we have given the modeling of the power spectrum of a single sample. With this model established, it is an easy step to the Fisher matrix for multiple samples. As explained in Section VII A, our SPHEREx forecasts divide the simulated galaxy catalog into redshift bins, and the sample at each redshift into subsamples with varying galaxy bias, based on redshift accuracy. To compute the Fisher matrix, we make the standard assumption of a Gaussian galaxy density field and assume the power spectra in different redshift bins are uncorrelated. Within each redshift bin, we use the information in all possible auto- and cross-power spectra of the different subsamples. The Fisher matrix element for parameters p_{α} and p_{β} thus becomes

$$F_{\alpha\beta} = \sum_{z_i} V(z_i) \int_{k_{\min}}^{k_{\max}} \int_{-1}^1 \frac{k^2 dk d\mu}{2(2\pi)^2} \text{Tr} \left[\mathbf{C}^{-1}(k, \mu; z_i) \frac{\partial \mathbf{C}}{\partial p_{\alpha}}(k, \mu; z_i) \mathbf{C}^{-1}(k, \mu; z_i) \frac{\partial \mathbf{C}}{\partial p_{\beta}}(k, \mu; z_i) \right] \exp \left[-k^2 \Sigma_{\perp}^2 - k^2 \mu^2 (\Sigma_{\parallel}^2 - \Sigma_{\perp}^2) \right] \quad (16)$$

(we set the fiducial cosmology equal to the reference cosmology). Here, $V(z_i)$ is the comoving volume in the z_i redshift bin. The $N_{\sigma_z} \times N_{\sigma_z}$ matrix $\mathbf{C}(k, \mu; z_i)$ is the covariance matrix of the observed galaxy overdensity in the various redshift uncertainty ($\tilde{\sigma}_z$) bins, including shot noise. In other words, the element corresponding to redshift uncertainty bins j_1 and j_2 , and redshift bin z_i , is given by

$$\mathbf{C}_{j_1 j_2}(k, \mu; z_i) = \sqrt{P_{g, j_1}(k, \mu; z_i) P_{g, j_2}(k, \mu; z_i) + \delta_{j_1 j_2}^K \frac{1}{\bar{n}_{j_1}^g(z_i)}}, \quad (17)$$

where the power spectrum terms on the right hand side are to be taken from Eq. (12) applied to the galaxy bias and redshift scatter of subsamples j_1 and j_2 , and the shot noise is assumed to be Poissonian.

We compute this Fisher matrix for the following cosmological parameters,

$$p_{\alpha} = \{\omega_b, \omega_c, \omega_{\nu}, \Omega_{\text{DE}}, \Omega_K, n_s, \alpha_s, \sigma_8, w_0, w_a, f_{\text{NL}}^{\text{loc}}\}. \quad (18)$$

In addition, while the prescription of Section VIII B gives us an estimate of the galaxy bias (in the absence of non-Gaussianity) of each subsample, $b_{G, j}(z_i)$, we treat this galaxy bias as a free parameter, with the value based on Section VII B its fiducial value. This adds $N_z \times N_{\sigma_z}$ bias parameters, $b_{G, j}(z_i)$, to the Fisher matrix, which we marginalize over when calculating parameter uncertainties. The effects of cosmological parameters on the matter power spectrum, which is the main ingredient to the galaxy power spectrum, is obtained using CAMB [45]. For the range of scales included in the forecast, we use $k_{\min} = 0.001h/\text{Mpc}$ and $k_{\max} = 0.2h/\text{Mpc}$. Finally, we always include a Planck CMB prior to break parameter degeneracies. This prior encodes the information in the CMB angular power spectra, and does *not* include bispectrum information. Therefore, it does not provide any direct information on $f_{\text{NL}}^{\text{loc}}$.

D. Bispectrum methodology

In addition to the power spectrum described in the previous section, structure formation also imprints cosmological information in the higher order moments of the density field. Gravitational instability amplifies the initial perturbations non-linearly on small scales so that the three-point correlation function and its counterpart in Fourier space, the bispectrum, become non-zero. These three-point statistics are sensitive test of the gravitational instability paradigm but also of the galaxy biasing. They can be used to break the degeneracy between the linear bias and the matter

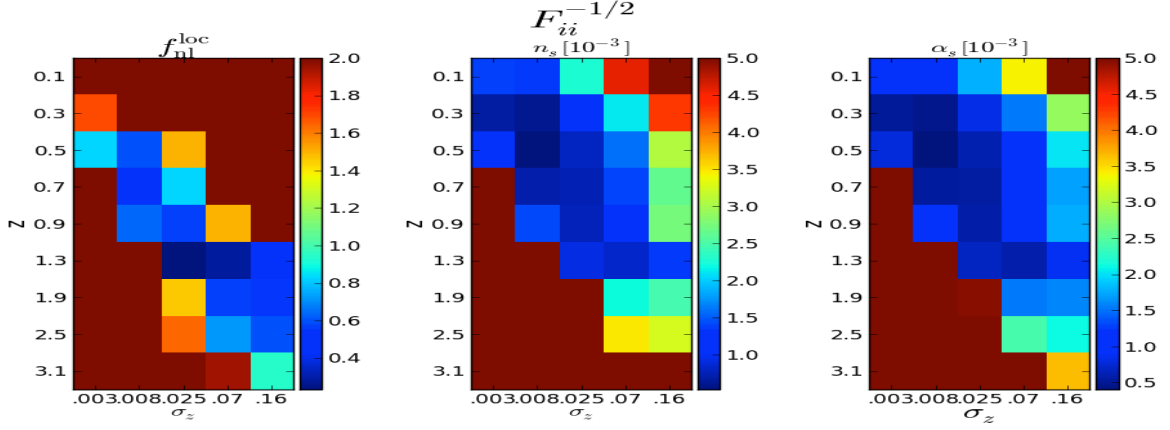


FIG. 12: Unmarginalized constraining power from the galaxy bispectrum in different bins in redshift and redshift accuracy. The horizontal axis shows the mean redshift scatter $\tilde{\sigma}_z = \sigma_z/(1+z)$ of each galaxy subsample. From left to right, constraining power is shown on $f_{\text{NL}}^{\text{loc}}$, n_s and α_s .

density parameter present in power spectrum measurements. In addition to the memory of the infationary bispectrum present in the initial conditions, their sensitivity to the bias make them very sensitivite probe of the primordial non-Gaussianity, in a complementary manner to the power spectrum. Most recently, the bispectrum has been measured using the SDSS DR11 data and lead to insightful constraints on the linear growth of structures [46, 47].

We will focus here on third-order statistics in form of the $3D$ galaxy bispectrum

$$\hat{B}_g(\mathbf{k}_1, \mathbf{k}_2, \mathbf{k}_3) = (2\pi)^3 \delta_{\text{D}}(\mathbf{k}_1 + \mathbf{k}_2 + \mathbf{k}_3) \hat{\delta}_g(\mathbf{k}_1) \hat{\delta}_g(\mathbf{k}_2) \hat{\delta}_g(\mathbf{k}_3), \quad (19)$$

which has the potential to probe interactions in the early Universe through measurements of the primordial bispectrum, and has considerable constraining power due to the enormous number of fundamental triangles contained in the survey volume.

We model the late-time galaxy spectrum as the sum of the primordial bispectrum and the tree-level bispectrum, which is caused by non-linear structure formation, modulated by non-Gaussianity induced scale-dependent galaxy bias. For local primordial non-Gaussianity, this can be written as

$$B_{g,j}(\mathbf{k}_1, \mathbf{k}_2; z_i) = \prod_{l=1}^3 b_j(k_l, z_i) \left\{ \left[\frac{\Omega_m H_0^2 k_3^2 T(k_3)}{k_1^2 T(k_1) k_2^2 T(k_2) D(z_i)} + 2F_2^{(s)}(\mathbf{k}_1, \mathbf{k}_2) \right] P_m(k_1; z_i) P_m(k_2; z_i) + 2 \text{ perm.} \right\} \\ + b_{2,j}(z_i) b_j(k_1, z_i) b_G(k_2, z_i) P_m(k_1; z_i) P_m(k_2; z_i) + 2 \text{ perm.}, \quad (20)$$

with $b_{2,j}$ the quadratic galaxy bias parameter of galaxies in redshift bin z_i and redshift scatter $\tilde{\sigma}_{z,j}$, which is determined analogously to Eq. 9, and where we have already imposed the triangle condition $\mathbf{k}_3 = -\mathbf{k}_1 - \mathbf{k}_2$. In this expression, the two terms in curly brackets describe the inflationary matter bispectrum propagated to redshift z and the tree-level matter bispectrum, the last term denotes the contribution from non-linear galaxy clustering with b_2 the quadratic galaxy bias. As in the power spectrum forecast, we calculate the covariance in the Gaussian approximation, so that different triangles configurations are uncorrelated, and the variance of each configuration is given by [48]

$$\text{Var}(B_{g,j}(\mathbf{k}_1, \mathbf{k}_2; z_i)) = V_{\text{survey}}(z_i) \left(P_{g,j}(k_1; z_i) + \frac{1}{\bar{n}_j^g(z_i)} \right) \left(P_{g,j}(k_2; z_i) + \frac{1}{\bar{n}_j^g(z_i)} \right) \left(P_{g,j}(k_3; z_i) + \frac{1}{\bar{n}_j^g(z_i)} \right). \quad (21)$$

The impact of redshift errors on the bispectrum is more complicated than in the power spectrum case, as each triangle side now has as a component along the line of sight. To simplify this calculation, we restrict the bispectrum Fisher matrix to triangle configurations with an an-isotropic upper limit $\mathbf{k}_{\text{max}} = (k_{\text{max}}, k_{\text{max}}, k(\tilde{\sigma}_{z,j}; z_i))$ on each Fourier mode in the triangle; here the limit perpendicular to the line of sight is given by the usual k_{max} determined by the scale at which tree-level modeling becomes inaccurate, and $k(\tilde{\sigma}_{z,j}; z_i) = 2\pi H(z_i)/(c\tilde{\sigma}_{z,j})$

$$F_{\alpha\beta} = \sum_{z_i} \sum_{\mathbf{k}_1} \sum_{\mathbf{k}_2} \Theta(k_{\text{max}} - k_3) \Theta(k(\tilde{\sigma}_{z,j}; z_i) - k_{3,z}) \frac{\partial B_{g,j}(\mathbf{k}_1, \mathbf{k}_2; z_i)}{\partial p_\alpha} \frac{1}{\text{Var}(B_{g,j}(\mathbf{k}_1, \mathbf{k}_2; z_i))} \frac{\partial B_{g,j}(\mathbf{k}_1, \mathbf{k}_2; z_i)}{\partial p_\beta}, \quad (22)$$

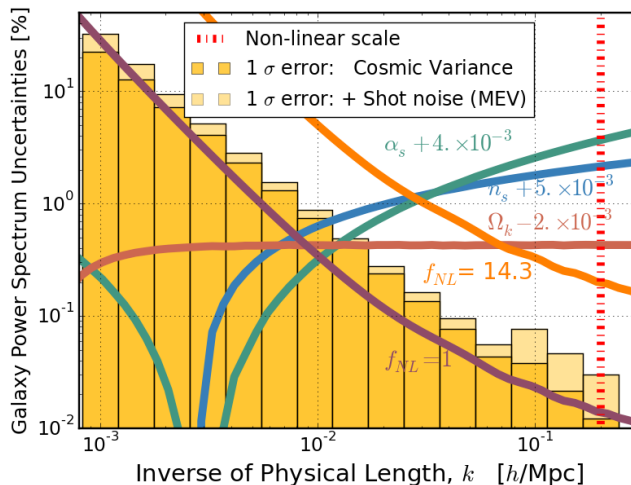


FIG. 13: SPHEREx relative errors for the galaxy 3-D power-spectrum as a function of wavenumber. The relative statistical and cosmic variance error bars correspond at the weighted combination of all redshift. The solid curves correspond to the theoretical model relative variation with regards to the fiducial one. The theoretical models are computed at $z = 1$.

where the binned sum over triangle sides is defined as

$$\sum_{\mathbf{k}} = \sum_{k_x=k_{\min}}^{k_{\max}} \frac{\Delta k_x}{k_F} \sum_{k_y=k_{\min}}^{k_{\max}} \frac{\Delta k_y}{k_F} \sum_{k_z=k_{\min}}^{k(\sigma_{z,i})} \frac{\Delta k_z}{k_F} \Theta(k_{\max} - k), \quad (23)$$

with $\Delta \mathbf{k}$ the bin width, which we choose as $\Delta \mathbf{k} = \tilde{\mathbf{k}}_{\max}/10$ for computational speed, and where the step function Θ restricts the analysis to $k < k_{\max}$.

For galaxy samples with non-negligible redshift uncertainties, a multi-tracer bispectrum analysis is computationally prohibitively expensive. Hence our Fisher matrix analysis includes one galaxy population per redshift bin, and we choose the $\tilde{\sigma}_j(z_i)$ as follows: In the cosmic variance limit, galaxy samples with $k(\sigma_z; z) \sim k_{\max}$ have the most constraining power due the rapid increase of the number of accessible triangles with $\tilde{\mathbf{k}}_{\max}$. However, for the SPHEREx galaxy selection function, the low redshift uncertainty galaxy samples become shot noise dominated near k_{\max} around $z \sim 1$, and the constraining power is higher for galaxy samples with lower shot noise (and higher redshift uncertainty), as illustrated in Figure 12.

E. Results

In practice, we divide the simulated catalog into five redshift accuracy bins, given by

$$\tilde{\sigma}_z \equiv \frac{\sigma_z}{1+z} = 0 - 0.003 - 0.01 - 0.03 - 0.1 - 0.2. \quad (24)$$

This leads to the cumulative comoving number densities shown in Figure 10 (the inset illustrates the distribution of the estimated redshift relative to the true redshift for each subsample). The number density in each subsample is of course given by the difference between subsequent curves. We now turn to the cosmological constraints that can be obtained with these samples, using the methods extensively discussed in the previous sections. It is useful to separate the discussion of the constraints on primordial non-Gaussianity from those on other parameters. The $f_{\text{NL}}^{\text{loc}}$ power spectrum constraints are driven by the largest scales available to the survey and, as a consequence, do not require high redshift accuracy. The suppression of information due to redshift scatter is such that almost the full power of the first four samples, i.e., up to $\tilde{\sigma}_z = 0.1$, can be used. While the suppression becomes large around $\tilde{\sigma}_z = 0.1$, even the $\tilde{\sigma}_z = 0.1 - 0.2$ bin still contributes to the final constraint. Thus, for $f_{\text{NL}}^{\text{loc}}$, we have a very deep sample at our disposal. The other parameters, on the other hand, rely strongly on the smallest scales accessible to the survey and to our modeling capabilities. Since the main focus of the SPHEREx cosmology program is inflation, we are here particularly interested in the parameters f_{NL} , n_s , α_s and Ω_k . In addition, we will be able to place tight bounds on the dark energy parameters w_0 and w_a , and on the sum of neutrino masses, Σm_ν . For all these parameters, the most important sample

is the highest redshift accuracy one, $\tilde{\sigma}_z < 0.003$ (i.e., nearly spectroscopic redshift quality for cosmology purposes), although the $\tilde{\sigma}_z = 0.003 - 0.01$ also contributes significantly, despite its relatively large suppression of information due to redshift scatter.

Starting with $f_{\text{NL}}^{\text{loc}}$, Figure 13 illustrates the amplitude of the scale-dependent bias signal for $f_{\text{NL}}^{\text{loc}}$ values at the level targeted by SPHEREx. While in practice, we use many redshift and redshift accuracy bins, the plot condenses down the information to a single effective redshift for illustration purposes. The error bars show the sensitivity of SPHEREx, with and without cosmic variance. The plot shows that the SPHEREx power spectrum measurement should be sensitive to $|f_{\text{NL}}^{\text{loc}}| \sim 1$. The results of the detailed Fisher forecast are shown in the first row of Table II. Indeed, we find that SPHEREx can reach $\sigma(f_{\text{NL}}^{\text{loc}}) = 0.87$. The second column shows that the galaxy bispectrum can reach significantly higher precision, with the best possible SPHEREx bound coming from the combination of the two (third column). The EUCLID column shows the constraint expected from the EUCLID spectroscopic galaxy clustering analysis, computed with the same power spectrum forecast method as used for SPHEREx. We do not show EUCLID bispectrum forecasts as they do not exist yet. Finally, the last column shows the current $f_{\text{NL}}^{\text{loc}}$ constraint from the Planck CMB bispectrum [9]. Based on these forecasts, even with the galaxy power spectrum only, we thus expect an $f_{\text{NL}}^{\text{loc}}$ bound a factor ~ 6 better than the expected constraint from the EUCLID spectroscopic sample, and a similar factor with respect to the current CMB-based bound. When taking into account the bispectrum, the improvement over EUCLID is substantially more.

1σ errors	PS	Bispec	PS + Bispec	EUCLID	Current
$f_{\text{NL}}^{\text{loc}}$	0.87	0.23	0.20	5.59	5.8
Tilt $n_s (\times 10^{-3})$	2.7	2.3	2.2	2.6	5.4
Running $\alpha_s (\times 10^{-3})$	1.3	1.2	0.65	1.1	17
Curvature $\Omega_K (\times 10^{-4})$	9.8	NC	6.6	7.0	66
Dark Energy FoM = $1/\sqrt{\text{DetCov}}$	202	NC	NC	309	25

TABLE II: Forecasted constraints from SPHEREx on inflationary parameters and on the dark energy figure of merit (FoM). See text for details. Estimates of current constraints and future constraints from the EUCLID spectroscopic galaxy survey are shown for comparison. NC stands for “Not Calculated”.

Moving on to cosmology beyond primordial non-Gaussianity, the next rows in Table II show the expected constraints on the tilt n_s and running α_s of the primordial power spectrum, the spatial curvature of the Universe Ω_K , and the dark energy figure of merit (we here take $\text{FoM} = 1/\sigma(w_p)\sigma(w_a)$, where w_p is the dark energy equation of state at the pivot redshift). In all cases (including $f_{\text{NL}}^{\text{loc}}$), we marginalize over all parameters of the vanilla Λ CDM model, $\omega_b, \omega_c, \Omega_\Lambda, n_s, \sigma_8, \tau$ (we remind the reader that we always include a CMB power spectrum prior to break parameter degeneracies) and over galaxy bias. For the prospected uncertainties on the inflation parameters n_s, α_s and Ω_K , we additionally marginalize over the full inflationary parameter space, including n_s, α_s, Ω_K and $f_{\text{NL}}^{\text{loc}}$. The estimates of current constraints beyond $f_{\text{NL}}^{\text{loc}}$ come from Planck CMB data for n_s (Table 5 of [49]), from Planck CMB plus a compilation of BAO measurements for α_s and Ω_K (Table 10 of [49]), and we base the dark energy FoM on the Planck + BAO $w_0 - w_a$ constraints in Table 15 of [50].

For parameters beyond $f_{\text{NL}}^{\text{loc}}$, we thus see that SPHEREx will deliver constraints comparable to those expected from the EUCLID spectroscopic survey. Since the SPHEREx constraints are driven by the low- $\tilde{\sigma}_z$ sample of SPHEREx, which is restricted to $z < 0.9$, SPHEREx provides information independent of and complementary to the EUCLID galaxies, which are at $z > 0.9$.

Figure 14 provides an illustration of the ability of SPHEREx to constrain the inflationary parameter space. SPHEREx will strongly narrow down the allowed parameter space in the $f_{\text{NL}}^{\text{loc}} - \alpha_s$ plane. Specifically, while single-field models predict negligible $f_{\text{NL}}^{\text{loc}}$ (in the squeezed limit) [51, 52], multi-field models generically generate $|f_{\text{NL}}^{\text{loc}}| \gtrsim 1$ [6, 53, 54]. Moreover, various non-primordial effects, such as “GR effects” and non-linear evolution, produce interesting cosmological signals equivalent to those of primordial non-Gaussianity of order $|f_{\text{NL}}^{\text{loc}}| \sim 1$. SPHEREx, with its sensitivity $\sigma(f_{\text{NL}}^{\text{loc}}) = 0.87$ from the power spectrum, and $\sigma(f_{\text{NL}}^{\text{loc}}) = 0.23$ from the bispectrum is thus in an excellent position to detect the non-primordial signal, and to distinguish between single- and multi-field models. Crucially, SPHEREx has two more or less *independent* measurements, since the bispectrum largely gets its information from different scales than the power spectrum, so that the new insights it will provide into the nature of inflation will be very robust. Finally, Figure 14 also shows that, by measuring α_s , SPHEREx will enable a stringent test of the class of slow-roll inflation models.

While *local* non-Gaussianity has a particularly striking effect on galaxy bias, because it appears on the largest scales and is weakly degenerate with other parameters (with regards to the galaxy power spectrum), other types of non-Gaussianity also leave a scale-dependent signature in the galaxy bias. While more detailed studies remain

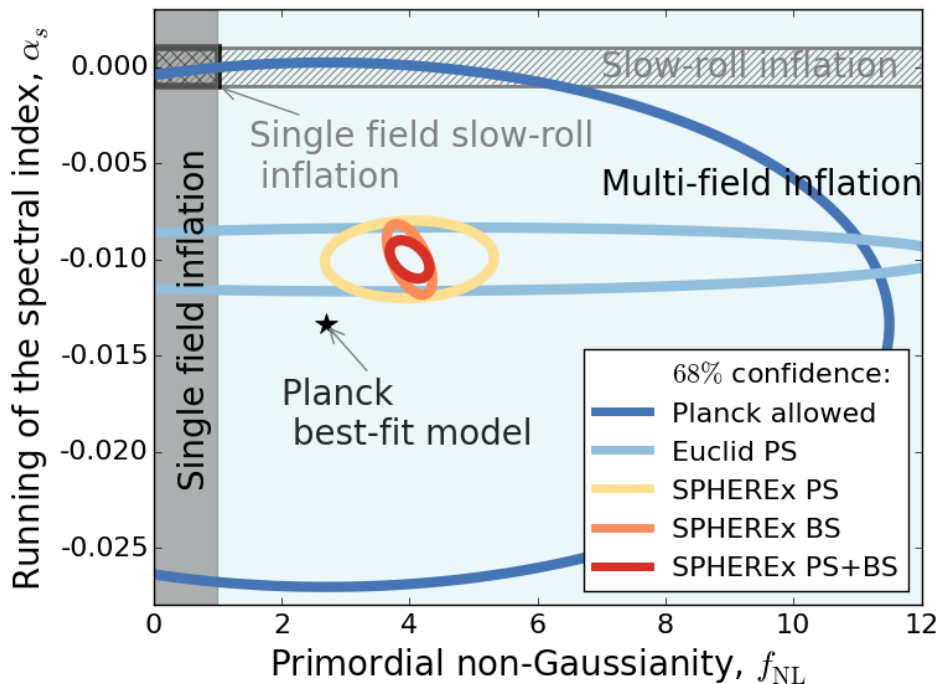


FIG. 14: 68% confidence level contours in the $f_{\text{NL}}^{\text{loc}}-\alpha_s$ plane from the SPHEREx power spectrum and bispectrum analyses. We show the constraints from current data and those expected from the EUCLID spectroscopic survey for comparison. Various areas of interest for inflation model classes are presented as well.

to be performed, we have carried out preliminary forecasts of how well SPHEREx will constrain non-Gaussianity of the equilateral type, parameterized by $f_{\text{NL}}^{\text{eq}}$. In this case, the scale-dependence of the bias correction is given by $\Delta b \propto 1/T(k)$, e.g., [55, 56], where $T(k)$ is the linear transfer function of matter perturbations normalized to unity at low k (large scales). Thus, the effect of equilateral non-Gaussianity is a bias correction at small scales, rather than large (since the k -independent contribution to the bias at low k is not observable). In the large- k limit, it scales like $\Delta b \propto k^2 \ln(k)$. Making the same assumptions as for the $f_{\text{NL}}^{\text{local}}$ calculations, our forecasts show that the SPHEREx galaxy power spectrum can reach a constraint $f_{\text{NL}}^{\text{eq}} \approx 7$. Our bispectrum forecasts suggest that the bispectrum can do at least as well on $f_{\text{NL}}^{\text{eq}}$ as the power spectrum. However, we note that because of the scale dependence in the equilateral case, $f_{\text{NL}}^{\text{eq}}$ has a much stronger degeneracy with other parameters, and perhaps more worryingly, with non-linear effects. A more robust forecast would take this into account by using a more detailed model of non-linear bias, non-linear evolution, and non-linear redshift space distortions.

VIII. SYSTEMATIC EFFECTS ANALYSIS

While the simulation suite described in Sec. VI provides a clear assessment of the statistical uncertainties in the SPHEREx all-sky galaxy clustering survey, it does not encompass any systematic effects associated with the unique scan strategy and spectral sampling techniques employed. In this section, we discuss and quantify the various systematic effects, both instrumental and astrophysical and the methods of mitigation. Of particular interest are the sources of error coherent on large angular scales ($\sim 10^\circ$), which introduce artificial correlations in the 3-D source catalogs. We estimate all sources of error must be controlled to 0.2% (rms per dex in wavenumber) to measure $f_{\text{NL}}^{\text{loc}}=1$. Table III provides a concise summary of the effects described below. The images in Figure 15 shows the various astrophysical components which can contribute systematics as they appear on the array.

- **Galactic Extinction** Variable atmospheric extinction has been a problem for past $f_{\text{NL}}^{\text{loc}}$ studies (e.g., [57]) SPHEREx avoids this by observing from space. Spatially variable galactic dust extinction leads to variations in depth of galaxy surveys if not corrected. It is an order of magnitude smaller at $3.2 \mu\text{m}$ (the $1.6 \mu\text{m}$ bump at $z=1$) than in the i -band. Standard extinction corrections and template projections have sufficient accuracy to remove this modest variation.

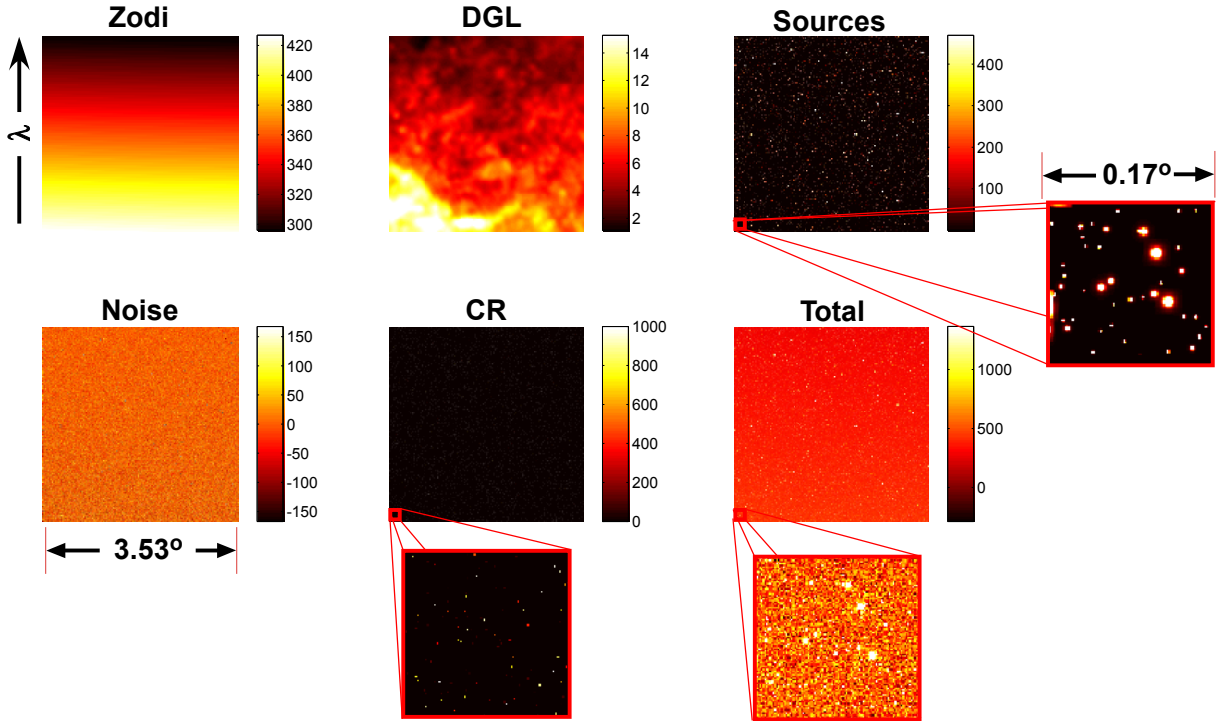


FIG. 15: Components of a single simulated SPHEREx exposure for the short wavelength band towards the region $[\alpha, \delta] = [16^h 11^m 36^s, +54^d 23^m 17^s]$. Color stretch indicates λI_λ and is given in units of $\text{nW m}^{-2} \text{sr}^{-1}$. Counter-clockwise from the upper right, the components show: a map of the unresolved sources, the Diffuse Galactic light, Zodiacal light, Noise (including contributions from read and photon statistics), cosmic rays, and the sum of all components. Insets show a subsection of the same images.

- Zodiacal light (ZL)** in the NIR arises from scattered sunlight by interplanetary dust in the optical and near-infrared (and thermal emission from the same dust in the mid- and far-infrared). For our baseline sensitivity we assume a sky brightness of $575 \text{ nW/m}^2 \cdot \text{sr}$ (0.24 MJy/sr) at $1.25 \mu\text{m}$. According to the DIRBE/Kelsall ZL model, this brightness corresponds to an ecliptic latitude of 20 degrees at a solar elongation of 90 degrees. This is empirically borne out by measurements of the total sky brightness in Figs. 16 borrowed from [59]. The discrepancy noted in right panel of Figs. 16 is largely due to residual star light which is not fully removed in the CIBER-LRS $1' \times 1'$ pixels. On a source by source basis, we find that the effect of ZL (and DGL) on optimal photometry (and thus redshift estimation) is negligible as both components appear as a slow gradient across the full image. Each images can provide a simple background gradient estimate to accurately remove the contribution from any such diffuse emission. The variation in ZL brightness (and DGL to a lesser extent) produces a variation in sensitivity in these background-limited images that will vary the selection function. We will handle it as discussed below.
- Diffuse Galactic Light (DGL)** in the NIR arises from the Galactic radiation field scattering off interstellar dust. While its absolute intensity is much less than the ZL for most of the sky, the spatial variation is on smaller angular scales more relevant to compact source extraction. To estimate the DGL in a SPHEREx FOV, we rely on the scaling relation between DGL intensity and $100 \mu\text{m}$ emission [58] including line emission from PAH features. Using this scaling relation as an input we simulate an expected field, as shown in the top center of Fig. 15 and combine it with estimates of all other effects discussed in this section, including simulated photon noise from all components. We then mask resolved sources and reconstruct the input DGL scaling relation. This is done for simulated maps of the sky as seen in 24 pointing centers scanned across the region as is done in the SPHEREx scan strategy. We find that using this technique, we were able to reconstruct the DGL to an RMS accuracy of $0.5 \text{ nW m}^{-2} \text{sr}^{-1}$, subdominant to the statistical noise by an order of magnitude. But to a large extent, this reconstruction is *not* necessary. Just as for ZL, the variation in DGL brightness will produce a small variation in sensitivity in these background-limited images that will vary the selection function and will be modeled as discussed below.

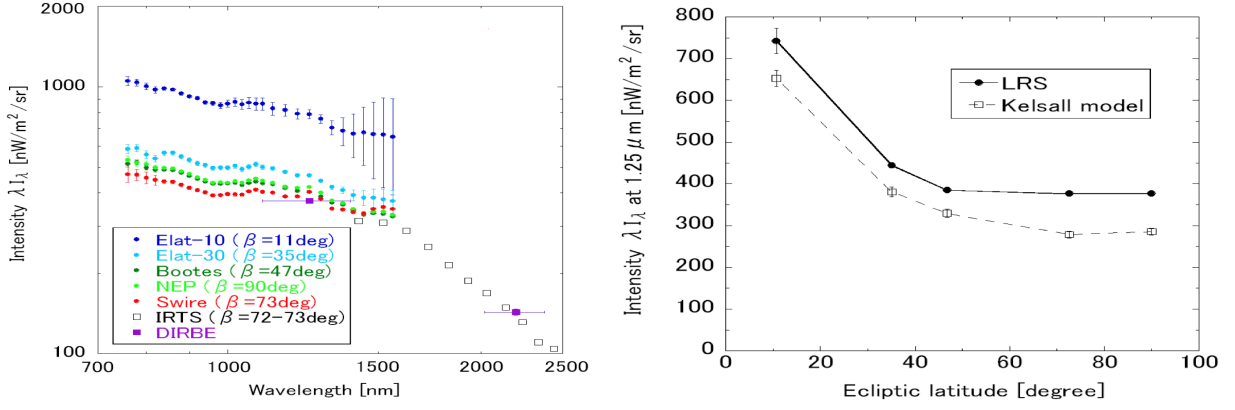


FIG. 16: Left: Measured spectra of the near-infrared sky brightness. Colored circles indicate the CIBER/LRS data used in [59], open squares indicate IRTS data averaged at 72 deg.-73 deg. ecliptic latitude from Matsumoto et al. (1996), and purple squares indicate darkest DIRBE data from Hauser et al. (1998). Right: Ecliptic latitude dependence of the DIRBE all-sky zodiacal dust model (Kelsall et al. 1998) (open squares) and the LRS sky brightness (circles) after partial removal of the integrated Galactic starlight based on detected stars at $\approx 1.25 \mu\text{m}$. There is still a residual from undetected stars that explains the observed difference. The impact from the difference of the solar elongation or ecliptic longitude should be small, because the range of them in our observation fields is narrow (<30 deg.; see Table 1) to see the ecliptic latitude dependence of the zodiacal light. The assumed ZL foreground in the SPHEREx sensitivity model is $575 \text{ nW/m}^2 \text{ sr}$ at $1.25 \mu\text{m}$. Note that $\sim 2/3$ of the sky area will have lower brightness than this assumed level, with somewhat better sensitivity than projected, while $\sim 1/3$ of the sky area will have higher brightness.

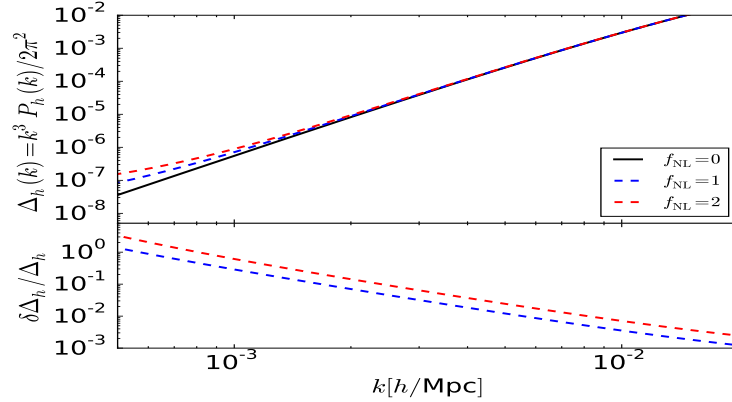


FIG. 17: Absolute (top) and fractional (bottom) power spectrum variation for the galaxy power spectrum at $z = 1$ for various $f_{\text{NL}}^{\text{loc}}$. To illustrate the required level of precision and systematics control for measuring $f_{\text{NL}}^{\text{loc}} \sim 1$, we plot the dimensionless power spectrum in the top panel, i.e. the variance in the galaxy overdensity per $\ln k$ interval.

- **Selection Non-Uniformity** Spatial variations in the selection function are introduced by changes in stellar density, sky brightness and noise level in the different fields (e.g., [60]). This effect will be characterized by simulations where artificial sources are injected into the real data pipeline to characterize the selection function. The same technique can be applied to understand the wavelength dependence of this selection function which can lead to spectral z non-uniformity. The understanding of this selection function will result in the definition of a non-uniform 3D weighting in the clustering analysis, just as is performed in 2D for full-sky survey with inhomogeneous noise such as WMAP or Planck.
- **Spectral Gain Errors** The gain between spectral channels is obtained by measuring the response to diffuse sky to inter-calibrate pixels within a spectral channel, and the 93 spectral standard stars observed over the sky (STSCI database). SPHEREx provides an excellent data set for measuring variations in gain response across the array as it is highly redundant and dithered at the celestial poles.
- **Flat Field.** The SPHEREx scan strategy provides an excellent data-set for measuring variations in gain response across the array (flat-field) as it is highly redundant and dithered at the celestial poles (deep regions). The self-

calibration algorithm of Fixsen, Moseley and Arendt 2000 will be applied to reconstruct the Gain matrices using the ZL as the flat-field source. Each day of Science operation, both celestial poles will be sampled 50 times for the deep survey. Assuming the Kelsall et al. [61] model for ZL intensity, the reconstruction of the flat-field will be accurate to 1.4% using data from a single day and accurate to 0.25% using one month of data.

- **Source Blending** We identify redshift targets from prior catalogs, and screen out blended galaxies using the higher-resolution WISE and Pan-STARRS/DES images. This method has been implemented successfully in previous selections of samples for spectroscopic follow-up by e.g., the Sloan Digital Sky Survey [62].
- **PSF Errors.** Flux extraction of unresolved sources using optimal photometry requires an accurate understanding of the PSF. For each wavelength in each exposure, we will generate a PSF template by stacking all stellar sources in the 2MASS catalog. Each spatial/spectral sample in SPHEREx spans a solid angle of 0.53 deg², for moderately high Galactic latitude fields, this will contain 350 stars with J-band magnitudes brighter than 14th. Simulations of this measurement have shown a PSF reconstruction accurate to a level of 1% on the FWHM of 1%. This technique is well established and has been previously demonstrated on science data [63]. We have simulated SPHEREx reconstructed PSFs with a systematic error of 1% on the FWHM, which produces an error of 0.1% on the inferred flux of a point source.
- **Absolute Pointing Reconstruction** To assess the worst case impact an imperfect pointing solution biases photometry result, we simulate the measurement of a $M_{AB}(\text{I band}) = 17$ galaxy and rely on the centroiding of the object from SPHEREx data alone. Using all 90 independent measurements of the object, its location was fit for to a 0.035 rms level. Using a centroid incorrect by this amount for optimal photometry produces a 0.04% random bias.
- **Saturation** H2RG arrays have a well depth of approximately 1×10^5 e-. For bright sources, which will generate more electrons than this in a single exposure, the inferred flux will be extracted by line-fitting only the early frames of the exposure [63]. This technique will be implemented in firmware on board the spacecraft. A pixel will therefore only be truly saturated if this threshold is reached in fewer than 3 frames, accounting for the Neff of the SPHEREx PSF, this corresponds to an I-band AB mag of 5.3. For regions of moderate Galactic latitude, we expect ~ 20 objects this bright in each FOV.
- **Cosmic Rays** Investigations of the WPFC3 cosmic ray rate (using a similar detector at a similar altitude to SPHEREx) give a cosmic ray hit rate that is $\leq 0.1\%$ of pixels per minute of integration [64, 65]. Estimates for the JWST H2RG [66][127] yield a cosmic ray rate where $\leq 1\%$ of pixels are affected in a 200s integration, which due to the different radiation environment at L2 we regard as conservative. Affected pixels are flagged and removed from later analysis.
- **Image Persistence** Previous measurements of persistence curves in H2RGs have demonstrated reproducible results at 0.02% accuracy over extended periods of time [67]. For the relevant timescales associated with the SPHEREx scan cadence and the expected bright star counts, we estimate roughly 20 pixels will need to be discarded in each exposure due to excessive image persistence from the previous exposure.
- **Dark Current Correction.** The H2RG detectors implemented by SPHEREx have demonstrated excellent dark current (DC) performance with a mean level of $0.02e^-/s$ and a one sigma spread of $0.005e^-/s$. This dispersion is negligible compared with the $\simeq 0.070 e^-/s$ statistical noise per pixel in a given image. Based on previous measurements of H2RG thermal stability (Finger et al. 2008), we conservatively estimate a maximum 10% variation in DC mean level. Additionally, as was implemented for the CIBER-LRS (Tsumura et al. 2013), where small regions of each array were masked to maintain a constant monitor of DC drifts, SPHEREx will use dark reference pixels provided in the H2RG design.

The formalism used to convert sky variations in the redshift estimator to galaxy overdensities, $\delta n/n$, is given in Appendix A. The fractional variation of the galaxy/halo density as a function of f_{NL}^{loc} is shown in Figure 17.

To conclude, to constrain primordial non-Gaussianity at the $f_{NL} \simeq 1$ level requires to accurately measure the largest scales on the sky, which in turn requires an exquisite control of systematic effects. SPHEREx design uniquely enables this control. The high-redundancy, the stability enabled by space will allow abundant cross-checks. The ability to infer redshifts from 97 bands from the same instrument in space, i.e., without the large scale fluctuations created by the atmosphere is unique amongst current or planned surveys.

Systematic	Mitigation	Amplitude	Conversion to $\delta n/n$	Technique	Coherent on large scales?	$\delta n/n$ % rms/dex
Galactic extinction	Observe in NIR, template projection	0.007 mag rms before mitigation	0.92/mag	e.g., Pullen & Hirata 2013	Yes	0.064
Noise selection non-uniformity	Inject simulated objects into real data	Template projection 0.2 mag rms (before mitigation)	1.8×10^{-3} /mag	e.g., Huff et al. 2014	Yes	0.036
Noise spectral z non-uniformity	Inject simulated objects into real data	Template projection 0.2 mag rms (before mitigation)	0.46/mag	e.g., Huff et al. 2014	Yes	0.092
Spectral gain errors	Measure flat field, calibrate on spectral standards	≤ 0.25 % pixel-pixel gain	NA	Fixsen et al. 2000	No	NA
Source blending	High resolution Pan-STARRS/ DES/ WISE catalog	Negligible for bright sources	NA	Jouvel et al 2009	No	NA
PSF and Astrometry Error	Stack on 2mass catalogs	$\leq 0.1\%$ flux	1	Zemcov et al. 2013	No	0.10
Cosmic Rays	Flag contaminated pixels	$\leq 1\%$ pixels lost/exposure	NA	Russell et al. 2009	No	NA
Bright Sources	Mask persistent pixels	$\leq 2\%$ pixels lost/exposure	1	Smith et al. 2008	Yes	0.04
Dark Current	Thermal stability	$\leq 10\%$ of statistical error	NA	Zemcov et al. 2013	No	NA

TABLE III: Main systematic effects in the SPHEREx inflationary science data analysis, their mitigation method with heritage and their impact on the galaxy over-density ($\delta n/n$) before and after mitigation. Adding the residuals errors of the last column in quadrature we obtain a 0.160% rms per dex which gives us a margin of 0.121 over our 0.2% rms per dex goal.

IX. SPHEREX SYNERGIES WITH EUCLID AND WFIRST

SPHEREx will enable new scientific opportunities in conjunction with Euclid [68] and WFIRST [69] datasets, largely as a result of the complementary redshift coverage (see Figure 11). In the following we highlight the most prominent examples.

A. SPHEREx - Euclid

Euclid is an ESA led satellite mission aiming to constrain dark energy through a combination of wide-field imaging and spectroscopy. The imaging component of Euclid encompasses 15,000 deg² to a nominal depth of 24.5 mag in one broad filter band (550-900nm) aiming at precision shape measurements for weak gravitational lensing (WL). Spectroscopic information, i.e., the galaxy clustering (GC)/baryonic acoustic oscillations (BAO) survey, will only be available for 1/30 of the WL galaxies [68].

The combination of sophisticated imaging from Euclid and high-precision redshift information from SPHEREx will greatly enhance the cosmological constraining power of Euclid WL by substantially improving on photo- z uncertainties and catastrophic photo- z errors. Removing these uncertainties is critical to Euclid’s cosmological constraining power. Since Euclid’s spectroscopic component will only cover 1/30 of its WL galaxies and the broad-band imaging prohibits an internal photo- z estimation, Euclid relies on ground based coverage in multiple bands to the same depth and over the full survey in order to determine its galaxy redshift. Although SPHEREx is more shallow than Euclid, it will improve Euclid’s overall photo- z estimation through cross-calibrating photo- z ’s using clustering information [70–72]. More importantly it will resolve potential catastrophic photo- z outliers at low redshifts, where their occurrence is most frequent and their impact most severe (see Figure 18). The improved photo- z estimation affects all of Euclid WL science; in addition to the increase in cosmological constraining power from cosmic shear, it also improves the cluster weak lensing signal and removes all confusion about cluster member galaxies and background galaxies from clusters below $z = 1$.

Most importantly perhaps the SPHEREx-Euclid data set will also enable new science via high precision galaxy-galaxy lensing measurements. Galaxy-galaxy lensing, i.e., the (stacked) shear signal of background galaxies (from high-precision Euclid WL) around the position of foreground galaxies (with high-precision redshift information from SPHEREx), allows for a direct measurement of the dark matter environment surrounding the foreground galaxies. This technique unlocks a number of interesting science studies that are not (or only to a much lesser precision) accessible when using the individual data sets.

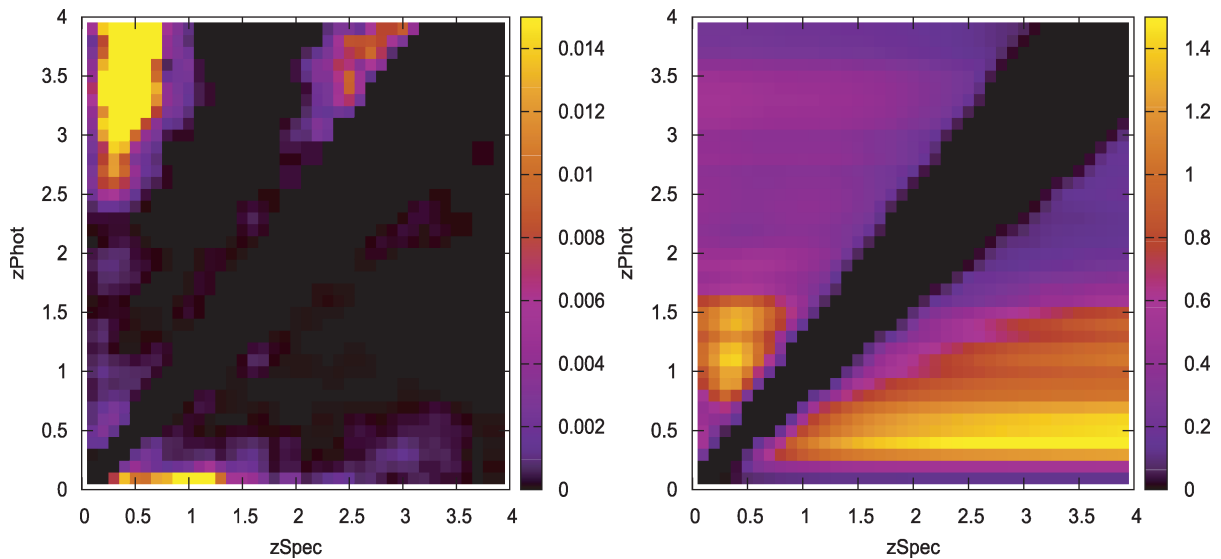


FIG. 18: *Left:* Contamination fraction of catastrophic photo- z per unit redshift in spectro- z (considered a good proxy for the true redshift of a galaxy). For a perfect photo- z survey, this plane should be empty. However, we see that some prominent contamination is happening for $z_{phot} > 2.5$ and $z_{phot} < 0.2$. The highest contaminations are at $z_{phot} > 2.5$, $z_{spec} < 0.6$ which are likely caused by confusion of high- z Lyman breaks with low- z $0.4 \mu\text{m}$ breaks. Note that a small leakage from shallow $z \sim 0.5$ galaxies can have a large impact on true galaxies at $z > 2.5$ since the latter are relatively rare. *Right:* The subsequent bias on dark energy parameters w_0 , w_a from catastrophic photo- z errors (bright regions indicate severe bias). The plot indicates that the outlier contamination rates must be known to one to three parts per thousand over all photometric redshift bins, most sensitively at $0.3 < z_{phot} < 1.5$ (Credit: [73]). SPHEREx high-precision redshift measurements at $z < 1$ will resolve the confusion of high and low redshift galaxies.

- **Study the Galaxy-Halo Connection** as a function of galaxy luminosity, type, and environment. Galaxy-galaxy lensing measurements allow for constraints on the luminous (stellar) mass with respect to the surrounding dark matter halo of the galaxy. These studies are extremely valuable for galaxy formation and evolution theories.
- **Intrinsic alignment of source galaxies.** A major astrophysical uncertainty for Euclid WL is the intrinsic alignment (IA) of sources, which mimics a WL signal and can substantially bias the inferred cosmological information. Overlapping imaging (from Euclid) and (near-) spectroscopic information (from SPHEREx) allows for measuring and removing the IA contamination from the WL signal ([74], [75]). This again will be limited to low redshift galaxies ($z < 1$), which however covers the redshift range where the IA contamination is damaging.
- **Baryonic physics inside Halos** The role of baryons in structure formation and the exact physical mechanisms associated with baryons is a fascinating topic in astrophysics and an extremely worrisome uncertainty in cosmological parameter estimation (e.g., [76], [77], and references therein). The impact of Baryonic Cooling, AGN, and SN feedback on the halo concentration parameter and the matter power spectrum can be constrained with galaxy-galaxy lensing.
- **Constrain Galaxy Bias** The combination of galaxy clustering and galaxy-galaxy lensing allows for constraints on the galaxy bias and thereby removes the largest uncertainty from galaxy clustering as a cosmological probe when inferring the matter power spectrum. This joint signal can be used as a cross-check for the matter power spectrum inferred from cosmic shear, or if in agreement the combination of all three probes can be used to substantially increase cosmological constraining power (e.g., [78], [79], and references therein).
- **Modified Gravity Studies** [80] use the combination of galaxy-galaxy lensing and galaxy clustering to build an estimator that constrains modified gravity theories on very large scales. Their analysis comprised $\sim 70,000$ large red galaxies only; the combination of Euclid and SPHEREx will allow for a substantial improvement in these constraints.
- **Higher-order moments of the density field** Galaxy-galaxy-galaxy lensing ([81]) is a powerful tool to investigate higher-order correlations of the density field, in particular whether this correlation varies as a function of galaxy type and luminosity ([82]).

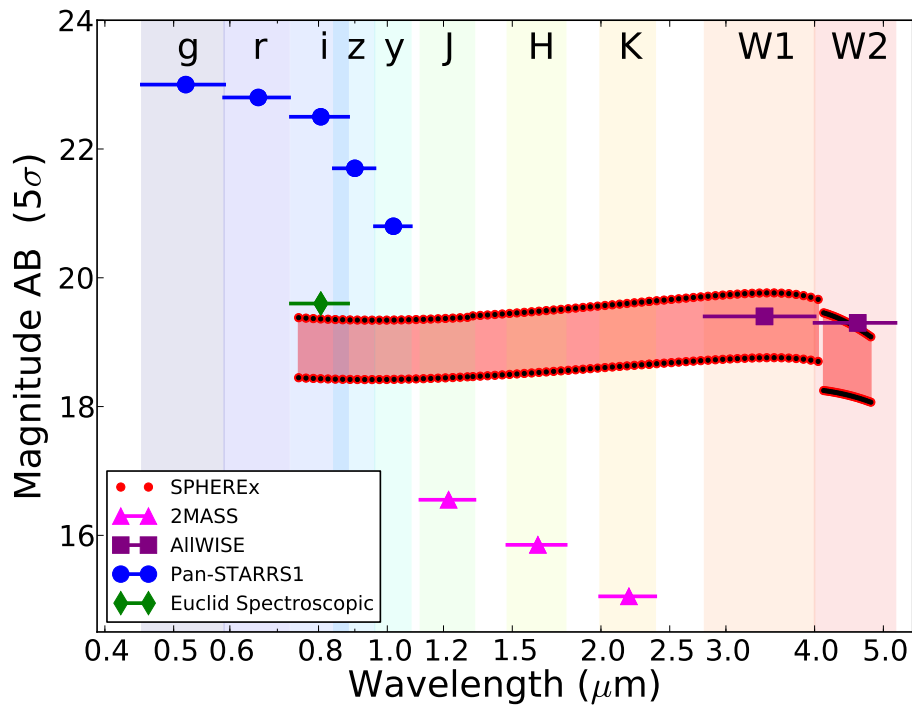


FIG. 19: SPHEREx all-sky survey depth as a function of wavelength compared to other large scale cosmological survey. Each red dot corresponds to one of SPHEREx 97 wavelength element. The top red curve corresponds to the current best estimate sensitivity while the bottom curve corresponds to the instrument sensitivity based on specifications that each sub-system can meet with contingency.

The precision of these studies strongly depends on the accuracy to which the lens redshift is known, hence the high-precision low- z information from SPHEREx combined with the Euclid shapes of background sources is an ideal data set for these science cases.

B. SPHEREx-WFIRST

The exact details of the WFIRST multi-band and grism instrumentation are still being determined, however most of the synergies outlined in the previous section apply very similarly to WFIRST. In the following we want to point out additional properties of a joint WFIRST-SPHEREx data set:

- A novel science case will be enabled by the combination of the unprecedented high-redshift and low-redshift cosmological volumes mapped by WFIRST and SPHEREx respectively. Jointly analysing the two samples will enable new cosmological measurements, probing directly the longest line-of-sight modes [83]. Comparing these line-of-sight modes with the modes perpendicular to the line-of-sights will enable potent new tests of general relativity on cosmological scales and test the isotropy hypothesis [84].
- The depth of the WFIRST mission causes it to be more susceptible to catastrophic photo- z confusion between high and low redshift (see Figure 18). Although WFIRST's instrumentation requirements will certainly take this into account, the mission will benefit from SPHEREx high-precision redshift measurements.
- The high number density of background galaxies enables a higher signal-to-noise ratio for the galaxy-galaxy lensing and cluster lensing measurements from the joint WFIRST-SPHEREx data set compared to the Euclid-SPHEREx case.

X. SPHEREX ALL-SKY SPECTRAL DATA-BASE LEGACY SCIENCE

All-sky surveys (IRAS, WMAP, Planck, WISE) have played a major role in advancing modern astrophysics, enabling ground-breaking science and producing versatile legacy archive that will prove valuable for decades. SPHEREx will

contribute to this proud heritage by carrying out the first all-sky spectroscopic survey at near-infrared wavelengths.

SPHEREx will measure the spectrum of every object in the 2MASS PSC (1.2 μm , 1.6 μm , 2.2 μm) catalog to at least (20σ , 40σ , 120σ) per spectral channel (see Figure 19). Most objects in the WISE catalog will also be detected by SPHEREx spectroscopically, the faintest detected at $\simeq 3\sigma$ in each spectral channel. Thus the SPHEREx data will contain high quality spectra of hundreds of millions of WISE and 2MASS sources, as well as a significant population of unique SPHEREx source detections at 1-3 μm . Such a rich archival spectral database will support numerous scientific investigations (e.g., Table IV) of great interest to the wider scientific community. We outline below a few examples.

SPHEREx enables new studies of galaxy formation. The entire catalog will contain 120 million galaxies with $\sigma(z)/(1+z) < 0.03$, sufficient for statistical galaxy evolution studies [15], and enabling clustering studies that link galaxy properties to their underlying dark matter haloes [85]. Importantly, SPHEREx will provide the first statistically significant spectroscopic dataset in the important 1-4 μm wavelength range. In local galaxies, SPHEREx will detect infrared diagnostic lines such as CO, H₂O, SII, and PAH emission that probe the interplay of stellar populations and AGNs with the density and excitation of the ISM. At higher redshifts, SPHEREx probes the H α , H β , O[III], and O[II] lines. In individual bright galaxies these spectra will find objects with unusually strong emission lines, due to AGNs or very low metallicities, and identify rare interesting objects such as quasars or heavily obscured sources. In fainter objects SPHEREx spectra allow ensemble studies of metallicity, obscuration and star formation over a wide range of redshifts and galaxy types.

As another example, a spectral catalog of main sequence stars over the entire sky opens numerous opportunities, e.g., a search for strong near- infrared excesses due to warm circumstellar dust radiating shortward of 5 μm . Large amounts of such dust signal catastrophic transient processes in an exoplanetary system orbiting the star. Kennedy & Wyatt (2013) estimate that such excesses should be seen around $\simeq 1\%$ of young stars and around 0.01% of stars older than 1 Gyr. Confirming these predictions and studying the nature of systems with recently injected dust would increase our understanding of planetary system evolution and tie exoplanet observations to events, such as the collision thought to have scooped the moon out of the Earth, which occurred in our Solar System.

XI. THE SPHEREX GALACTIC ICE INVESTIGATION

SPHEREx will carry out a groundbreaking survey of water and other biogenic ices in the Milky Way. By exploiting an optimal spectral region for ice spectroscopy, and increasing by 100-fold or more the number of ice spectra toward molecular clouds, young stellar objects and protoplanetary disks, the SPHEREx Galactic Ice Investigation will resolve long-standing questions about the amount and evolution of such biogenic molecules as H₂O, CO, CO₂, and CH₃OH, through all phases of star and planet formation. In this Section we describe the SPHEREx Ice Investigation technique, targets, data products, and science.

A. Introduction

Based on the fewer than 250 existing near- and mid-infrared absorption spectra toward Galactic molecular clouds, circumstellar envelopes, and protoplanetary disks (see Fig. 20) there is clear evidence that: (1) ices are common in dense (i.e., $n(\text{H}_2) \geq 10^3 \text{ cm}^{-3}$), well-shielded regions; (2) they accumulate in measureable quantities on the surface of dust grains; and, (3) for some important biogenic molecules, such as water (H₂O), carbon dioxide (CO₂), and methanol (CH₃OH), there is evidence that the amount of these species locked in ice, while variable from source to source, far exceeds that in the gas phase [88–90].

Why is this important? It has long been known that star formation occurs within the cores of dense interstellar clouds and that the gas and dust within these cores are the reservoirs from which stars and planets subsequently assemble. In young protoplanetary disks, both models and the limited amount of data presently available suggest that most of the water and, perhaps, other biogenic molecules, are locked in ice toward the disk mid-plane and beyond the snow line [Fig. 20; 91]. A recent theoretical study [e.g., 92] goes further and finds that much of the solar system’s water was likely inherited directly from interstellar ices, with little further processing in the pre-solar disk.

It is not known, however, whether the link between interstellar water ice and water in our own solar system is correct and typical of most planet-forming disks, or whether the ice composition in clouds and disks varies broadly. This ignorance is largely the result of the limited data currently available. To date, the *Infrared Space Observatory (ISO)*, *Spitzer*, and *AKARI* have obtained spectra in 10s of lines of sight toward a few dense clouds while an additional ~ 100 lines of sight have been probed toward protostars using *Spitzer* and *ISO*, revealing a highly variable ice composition [88]. The number of ice observations toward protoplanetary disks is much lower [e.g., 93, 94] because of the low disk inclination required for ice absorption studies.

Object	# Sources	Legacy Science	Reference
Detected galaxies	1.4 billion	Properties of distant and heavily obscured galaxies	Simulation based on COSMOS and Pan-STARRS
Galaxies with $\sigma(z)/(1+z) < 0.1$	301 million	Study large scale clustering of galaxies	Simulation based on COSMOS and Pan-STARRS
Galaxies with $\sigma(z)/(1+z) < 0.03$	120 million	Study (H α , H β , CO, OII, OIII, SII, H $_2$ O) line and PAH emission by galaxy type. Explore galaxy and AGN life cycle	Simulation based on COSMOS and Pan-STARRS
Galaxies with $\sigma(z)/(1+z) < 0.003$	9.8 million	Cross check of Euclid photo- z . Measure dynamics of groups and map filaments. Cosmological galaxy clustering, BAO, RSD.	Simulation based on COSMOS and Pan-STARRS
QSOs	> 1.5 million	Understand QSO lifecycle, environment, and taxonomy	Ross et al. [86] plus simulations
QSOs at $z > 7$	0-300	Determine if early QSOs exist. Follow-up spectroscopy probes EOR through Ly α forest	Ross et al. [86] plus simulations
Clusters with ≥ 5 members	25,000	Redshifts for all eRosita clusters. Viral masses and merger dynamics	Geach et al. [87]
Main sequence stars	> 100 million	Test uniformity of stellar mass function within our Galaxy as input to extragalactic studies	2MASS catalogs
Mass-losing, dust forming stars	Over 10,000 of all types	Spectra of M supergiants, OH/IR stars, Carbon stars. Stellar atmospheres, dust return rates, and composition of dust	Astro-physical Quantities, 4th edition [ed. A.Cox] p. 527
Brown dwarfs	>400, incl. >40 of types T and Y	Atmospheric structure and composition; search for hazes. Informs studies of giant exoplanets	dwarfarchives.org and J.D. Kirkpatrick, priv. comm.
Stars with hot dust	>1000	Discover rare dust clouds produced by cataclysmic events like the collision which produced the Earth's moon	Kennedy & Wyatt (2013)
Diffuse ISM	Map of the Galactic plane	Study diffuse emission from interstellar clouds and nebulae; hydro-carbon emission in the 3 μ m region	GLIMPSE survey (Churchwell et al. 2009)

TABLE IV: SPHEREx spectral database populations

B. Hundreds of Thousands of Ice Absorption Spectra

The vast majority of objects with rich ice absorption spectra are concentrated towards the galactic plane, so the SPHEREx Ices Survey nicely exploits the portions of the orbit that are inappropriate for extragalactic work. However,

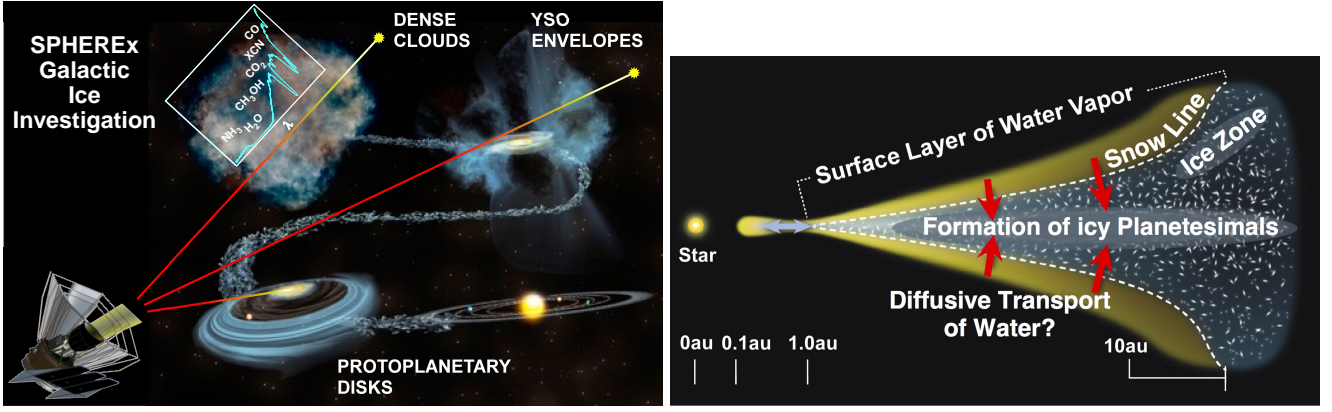


FIG. 20: Left: Evolutionary stages of star and planet formation. SPHEREx will obtain absorption spectra against more than 20,000, and as many as 10^6 , background stars and hundreds of protostars to reveal the ice content of these regions. Right: Schematic of a young protoplanetary disk showing the model-predicted zones of gas-phase water and water ice. Most of the water ice is expected to lie in the disk mid-plane beyond the snow line. SPHEREx will observe hundreds of protoplanetary disks with inclinations low enough to permit absorption spectroscopy against the central star.

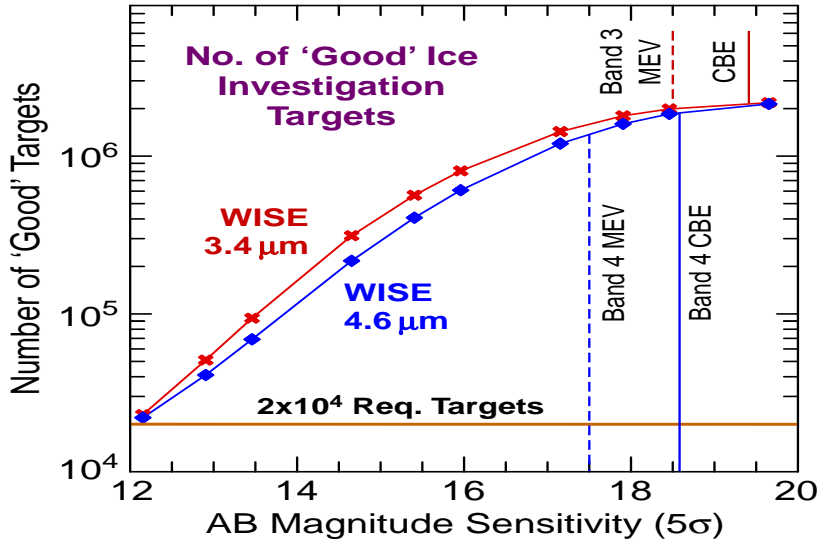


FIG. 21: Number of $3.4 \mu\text{m}$ and $4.6 \mu\text{m}$ point sources detected by WISE within $\pm 1^\circ$ of the Galactic plane that satisfy the criteria described in the text. The required 20,000 high-quality absorption spectra are realized with a Band 4 sensitivity of 12 AB mag (5σ) per spectral channel. The MEV performance set by the Inflation investigation at $\lambda < 4.1 \mu\text{m}$ and the Ice investigation at $\lambda > 4.1 \mu\text{m}$, will result in the detection of more than 10^6 targets.

to conduct a survey based on absorption spectroscopy, strong background point sources are required that are well separated and display evidence for extinction due to intervening material. Here we describe the SPHEREx strategy for identifying promising spectroscopy targets for the Ices Survey.

Our strategy relies on a combination of all-sky, near-infrared catalogs from the 2 Micron All-Sky Survey [2MASS; 95] and the Wide-field Infrared Survey Explorer [WISE; 12]. As a starting point, we begin with the WISE catalog of $> 10^7$ $3.4 \mu\text{m}$ (W1) and $4.6 \mu\text{m}$ (W2) point sources within $\pm 5^\circ$ of the Galactic plane as a starting point. We assess the suitability of each WISE source for our science with the following four criteria:

First, the source fluxes measured in the WISE W1 and W2 bands must be greater than 100 times the projected SPHEREx (1σ) sensitivity per resolution element at both 3.4 and $4.6 \mu\text{m}$, allowing for high SNR spectra. Second, the source must carry $> 99\%$ of the total flux detected in the WISE W1 and W2 bands in a local box of 2×2 SPHEREx pixels of $6.2''$. Third, there must be evidence that the source lies behind an intervening molecular cloud and is heavily extinguished. For the identification of such anomalous reddening, we used the Rayleigh-Jeans color excess method [96] and only retained stars with an infrared color of $H - [W2] > 1.5$. Fourth, we applied a color cut based on $K - [W2]$

TABLE V: Solid-State Ice Features: $2.96 \mu\text{m} \leq \lambda \leq 4.8 \mu\text{m}$

Molecule	λ (μm)	$\Delta\nu$ (cm^{-1})	Vibration Mode	Band Strength ($10^{-17} \text{ cm molecule}^{-1}$)
NH ₃	2.96	45	-N-H stretch	1.1
H ₂ O	3.05	335	O-H stretch	20
-CH ₂ -, -CH ₃	3.47	~ 10	C-H stretch	$\sim 0.1 - 0.4$
CH ₃ OH	3.53	30	C-H stretch	0.76
CH ₃ OH	3.95	115.3	C-H stretch	0.51
H ₂ S	3.95	45	S-H stretch	2.9
CO ₂	4.27	18	C-O stretch	7.6
¹³ CO ₂	4.38	12.9	¹³ C-O stretch	7.8
H ₂ O	4.5	700	$3\nu_L$ and/or $\nu_2 + \nu_L$	1.0
“XCN”	4.62	29.1	CN stretch	~ 5
CO	4.67	9.71	¹² CO stretch	1.1
¹³ CO	4.78		¹³ CO stretch	1.3

After Gibb et al. 2004, *ApJ Suppl. Series*, 151, 35.

to reject the few unobscured stars that pass the $H-[W2]$ cut, i.e., very evolved (unobscured) stars which are red in $H-[W2]$ but not in $K-[W2]$.

These four criteria correctly identified 22 of the 24 stars behind quiescent molecular clouds previously observed by *AKARI* [97] and *ISO* [98]. As expected, the spatial distribution of these sources is well aligned with regions of high CO emission measured by *Planck*, concentrating near the galactic plane. Applied to the entire 2MASS+*WISE* database, these criteria identify over one million “good sources” within 1 degree of the galactic plane, providing a strong and robust lower limit on the number of SPHEREx lines of sight sampling dense interstellar clouds.

Large numbers of protoplanetary disk targets are important for this investigation because the presence of a disk leads to an orientation-dependent spectrum; only a fraction ($\leq 10\%$) may be sufficiently edge on to show an optimum absorption spectrum against the embedded central star. Protoplanetary surveys using both *Spitzer* and *WISE* find over 3000 young and forming stars, of which about 750 are in the early collapse and protostellar phase and another 1500 in the protoplanetary disk phase. Many of these objects are bright enough to enable SPHEREx spectra with $\text{SNR} > 100$ in every spectroscopic pixel; again, this is a lower limit to the total number of such objects to be sampled by SPHEREx’s unbiased survey, because the existing surveys are not unbiased. Thus there will be ample spectra to trace the evolution of ices from dense interstellar clouds through the stages of the star and planet formation.

With an orbit that covers the entire Galactic plane every 6 months, high sensitivity, and good spectral resolving power, SPHEREx will increase the sample of high-quality Galactic ice absorption spectra by 100-fold or more in an unbiased survey that includes a rich diversity of interstellar clouds, young stellar object (YSO) envelopes, and protoplanetary disks. Thus, the SPHEREx catalog of $> 2 \times 10^4$ ice spectra can be used to evaluate the relation between ice content and cloud evolutionary stage through to the protoplanetary phase in ways not possible with the limited sample of spectra available today. Moreover, the breadth and depth of the groundbreaking SPHEREx ice spectra catalog is sure to reveal new and exciting sources that will merit follow-up by JWST.

Finally, based on laboratory ice spectroscopy and existing observations of interstellar ices, the $2.5 - 5 \mu\text{m}$ region is the richest part of the electromagnetic spectrum for the study of ices. This wavelength region includes strong absorption features for the main ice constituents H₂O, CO, and CO₂ as well as chemically important minor constituents NH₃, CH₃OH, X-CN, ¹³CO and ¹³CO₂ (see Table XIB and Fig. 22). The SPHEREx spectral resolving powers were selected in order to ensure that these key features can be unambiguously distinguished from one another, i.e., no line blending that would make the assignment of a unique optical depth to each ice feature uncertain. This is achieved with $R = \lambda/\Delta\lambda = 40$ at $\lambda \leq 4.1 \mu\text{m}$, which is dominated by the very broad H₂O-ice feature, and $R = 150$ at $\lambda > 4.1 \mu\text{m}$, where R is set by the need to spectrally separate the “XCN” feature at $4.62 \mu\text{m}$ and CO feature at $4.67 \mu\text{m}$. This is illustrated in Fig. 23 in which the spectra obtainable with SPHEREx with $R = 40$ and $R = 150$ are shown superposed on the *ISO* spectra.

C. Interstellar, Circumstellar, and Protoplanetary Ices: Volatile Reservoirs and Chemical Factories

Within the well-shielded interiors of molecular clouds, ices are the main repositories of many molecules, but their composition is line-of-sight specific [98, 99]. However, these icy mantles are not merely passive volatile reservoirs, but are instead active sites of chemistry. For example, hydrogenation and oxygenation reactions form H₂O from O, and CH₃OH from CO [100, 101]. The exposure of interstellar ices to radiation is expected to create reactive radicals in the ice, which recombine to form complex organic molecules [102, 103].

Though disks are expected to inherit some pristine cloud material [92, 104], they are also chemically active based on direct observations of the trace gases [91, 99]. The limited data presently available prevent us from knowing whether the main reservoirs of volatiles during planet formation (i.e., grain ice mantles) also evolve [94]. However, the observed range of comet compositions in our Solar System indicates that ices do evolve [105]. Constraining these ice abundances is key to modeling planet formation as the snow lines for different species strongly affect the initial steps as well as the bulk and surface volatile and organic compositions of nascent planets forming at different disk locations [106–108].

D. The Impact of the SPHEREx Galactic Ice Investigation

SPHEREx will be a game changer for the study of interstellar, circumstellar, and protoplanetary disk ices. The tens of thousands of high-quality ice absorption spectra toward a wide variety of regions distributed throughout the Galaxy will reveal possible correlations between ice content and environment not possible with only 100s of spectra. For example, the influence of cloud density, internal temperature, presence or absence of embedded sources, external UV and X-ray radiation, elemental abundances (such as C/O ratio), gas-phase molecular composition, cosmic-ray ionization rate, and cloud evolutionary stage, among other factors, can be correlated with the ice content in a statistically significant way.

Based on isotopic composition, the Cleeves et al. [92] finding that terrestrial and cometary H₂O ice in the Solar System formed in situ in the protostellar cloud and survived intact (rather than undergoing modification) through the star formation process exemplifies the type of science SPHEREx will enable. SPHEREx spectra, when properly corrected for continuum extinction, can be analyzed quantitatively to determine the fractional abundance of water ice relative to the entire dust content along the line of sight. This can be done for targets at all steps in the evolutionary path from interstellar cloud to protoplanetary disk, and as a function of the numerous variables listed above. It might be found that the relative abundance of H₂O ice is fairly constant in many environments, which would be strongly supportive evidence for the survival of the original interstellar material into the cold icy regions of the forming planetary system and suggest as well that water (essential for life as we know it) should be widespread throughout exoplanetary systems.

E. Ice Survey Follow Up Capabilities

Within the SPHEREx team we have direct access to state-of-the-art laboratory ice spectroscopy and chemistry experiments at Harvard University (Co-I Öberg). The ice spectroscopy experiments will be used to generate libraries of

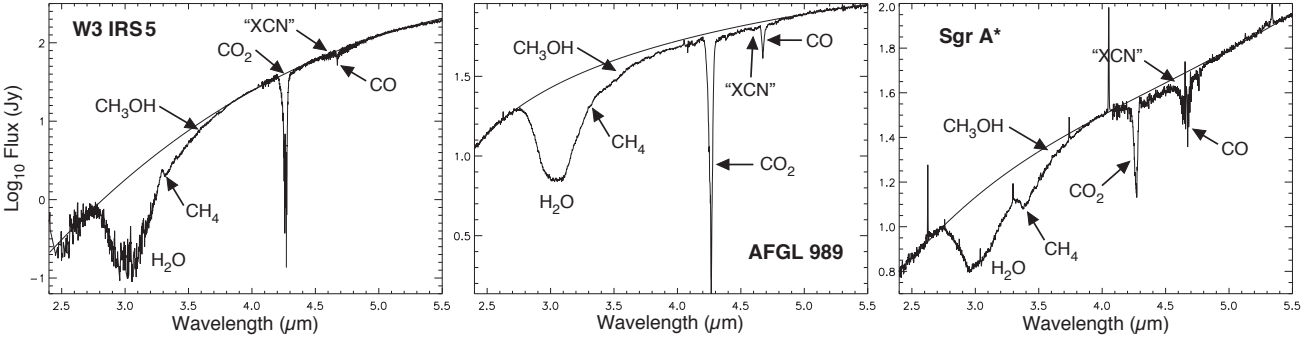


FIG. 22: Spectra toward a sample of Galactic star forming regions showing absorption features due to ices. These spectra were obtained using the Short Wavelength Spectrometer aboard the *Infrared Space Observatory* (ISO) with a spectral resolving power, $R = \lambda/\Delta\lambda$, of ~ 750 (Gibb et al. 2004, *ApJ Suppl. Series*, 151, 35).

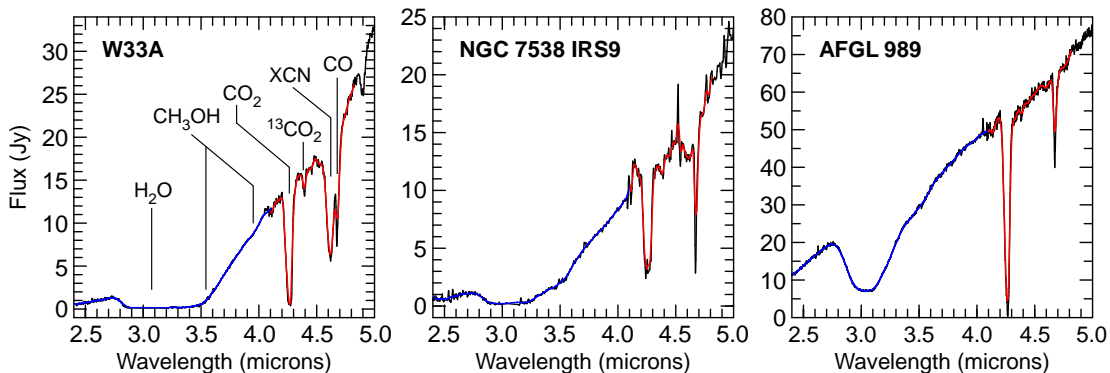


FIG. 23: Near-infrared spectra of two massive young stellar objects (YSO; W33A and NGC 7538 IRS9) and one intermediate mass YSO (AFGL 989) obtained by *ISO* with $R = 750$ (black line). The spectral region shortward of $4.1 \mu\text{m}$ has been smoothed to $R = 40$ (blue line) and between of $4.1 \mu\text{m}$ and $4.8 \mu\text{m}$ to $R = 150$ (red line). Because the solid-state ice features are inherently broad, little information is lost when sampling these spectra at R of 40 and 150 at $\lambda < 4.1 \mu\text{m}$ and $\lambda > 4.1 \mu\text{m}$, respectively. (Note: Unlike Fig. 22, these spectra are plotted on a linear scale to highlight the weaker features.)

ice (mixture) spectra as needed to interpret SPHEREx data and also to develop new tools to analyze ice spectroscopic data, using, e.g., different decomposition methods. The ice chemistry experiments will be used to test new ice formation and destruction pathways and how they relate to the local radiation field, aiding in the chemical interpretation of observed ice abundance and composition patterns. We also can use the Submillimeter Array at the CfA to follow up specific lines of sight using submillimeter observations of the gas-phase to obtain a more complete view of the volatile reservoir. For other targets, we will propose follow up with either ALMA or JWST, for which the the catalogue of SPHEREx ice spectra will be an invaluable resource.

XII. SPHEREX GALAXY EVOLUTION AND EOR INVESTIGATION

SPHEREx’s terminator orbit naturally accumulates observatory time at the celestial poles. We exploit this feature to produce two deeply mapped regions, enabling a unique large-scale measurement of spatial fluctuations in the extragalactic background light (EBL). These maps provide a novel probe of the origin and history of galaxy formation. The deep regions are also ideal for monitoring long-term instrument properties such as the flat-field response, gain, and noise performance.

A. Explaining the Extra-galactic Background Fluctuations with broad bands

EBL fluctuations trace the underlying clustering of faint emission sources, such as dwarf galaxies and intra-halo light (IHL), components not readily detected in point source surveys (Figure 24, left). The amplitude of the linear clustering signal is proportional to the total photon emission and thus an important tracer of star formation history. Near-infrared EBL fluctuations have been measured in broad continuum bands by a number of groups using AKARI [109], Spitzer [110, 110, 111] and CIBER [112]. The methods for these mapping measurements are well established. The fluctuation amplitude, robustly consistent across these experiments, exceeds that expected from the large-scale clustering of known galaxy populations [113]. While the spectrum of this excess is best described by low redshift emission such as IHL, other explanations have been proposed [114, 115]. The contribution from the first galaxies during the epoch of reionization (EOR) must be present in the background (Figure 24). SPHEREx has the sensitivity to determine the origin and history of the light production associated with EBL fluctuations, and search for an EOR component to minimum levels.

The measured near-infrared spectral energy distribution of EBL fluctuations (Figure 24, right) is well explained by diffuse IHL emission at low-redshifts ($z < 1$) arising from a population of stars no longer associated with their parent galaxies. When individual galaxies collide and merge, a fraction of the stars are stripped through dynamical friction to form an extended stellar halo. Indeed images of nearby galaxies show stars extending out to 300 kpc distances [117]. These stray stars lead to substantial IR fluctuations implying that IHL is a significant fraction of the background light [112, 118]. The exact spectral shape, and the degree of correlation between spectral bands, depends on stellar spectrum and the redshift history of IHL production. A sensitive multi-band fluctuations measurement thus can be

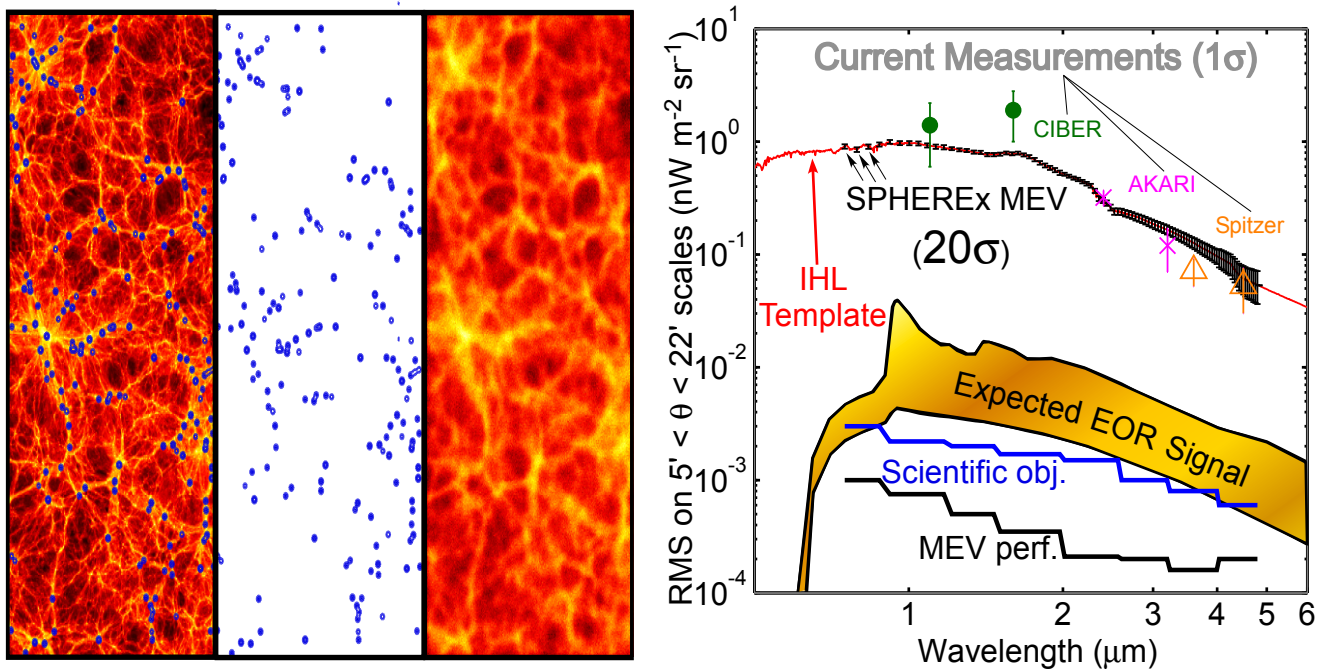


FIG. 24: Left: A large-scale mapping measurement like SPHEREx traces the total emission from diffuse components as well as the emission from individual galaxies. The left panel shows a numerical simulation of galaxies superposed with a diffuse emission component, such as IHL and early dwarf galaxies, that follows the structure of dark matter. A galaxy survey (middle) recovers the galaxies but misses the diffuse light component. A large-scale mapping measurement (right), traces the total emission from the diffuse component as well as the individual galaxies due to their clustering. Right: Amplitude of large-scale EBL fluctuations measured by CIBER, Spitzer, and AKARI, after removing the contribution from known galaxy populations. The solid lines show the expected IHL (red) and EOR (orange) signals. The bottom of the EOR range is the minimum signal that must be present given the existing $z > 7$ Lyman-break galaxy luminosity functions [116]. The top of the EOR range allows for fainter galaxies below the detection level of deep HST surveys. We show the MEV instrumental performance as the RMS between 5 and 22 arcmin in eight bands between 0.75 and 4.8 μm by the black lines.

used to probe the history of stars producing the IHL. EBL fluctuations contain the imprints of the first stars that ended the cosmic dark ages. Sometime between 200 Myr and 1 Gyr after the Big Bang ($z = 6-20$), the first collapsed objects formed and produced energetic UV photons that reionized the surrounding hydrogen gas. This EOR marks the end of the dark ages, and is the first chapter in the history of galaxies and heavy elements.

B. Line Intensity Mapping

The SPHEREx deep spectro-imaging survey also produces the ideal data set for full tomographic mapping of large-scale structure, a statistical study based on galactic emission lines. These emission lines trace linear large-scale galaxy clustering, but unlike 2D continuum measurements outlined above, provide 3D redshift information.

The spectral line intensity cubes from SPHEREx are an ideal tracer of galaxy evolution. At low redshifts SPHEREx will detect multiple lines with high signal to noise (Figure 25), the dominant lines being $\text{H}\alpha$ for redshifts $0.1 < z < 5$, $\text{H}\beta$ for redshifts $0.5 < z < 2$, and $[\text{OIII}]$ for redshifts $0.5 < z < 3$. At high redshifts $5.2 < z < 8$, SPHEREx accesses the $\text{Ly}\alpha$ line, providing a crucial probe of the formation and evolution of EOR galaxies. Traditionally $\text{H}\alpha$, after accounting for dust extinction, has been used as a reliable measure of the cosmic star-formation rate. In the deep SPHEREx region, we can measure the $\text{H}\alpha$ power spectrum in 10 redshift intervals, with $\text{SNR} > 100$ (Figure 25). The measurement of $\text{H}\alpha$ clustering thus traces bolometric line emission, integrated over all galaxy luminosities and including emission from any diffuse IHL component. Foreground line confusion from lower redshift $[\text{OIII}]$ and $\text{H}\beta$ lines can be robustly removed by cross-correlating spectral lines in multiple bands. For example, $z = 3$ $\text{H}\alpha$ line fluctuations are detected in a band centered at 2.62 μm , while at the same redshift $[\text{OIII}]$ fluctuations are present in a band centered at 2.00 μm . Cross-correlating two independent bands thus traces the galaxies at $z = 3$ without masking, and naturally rejects any line contaminants that may be present in one of the two bands. Intensity mapping at high

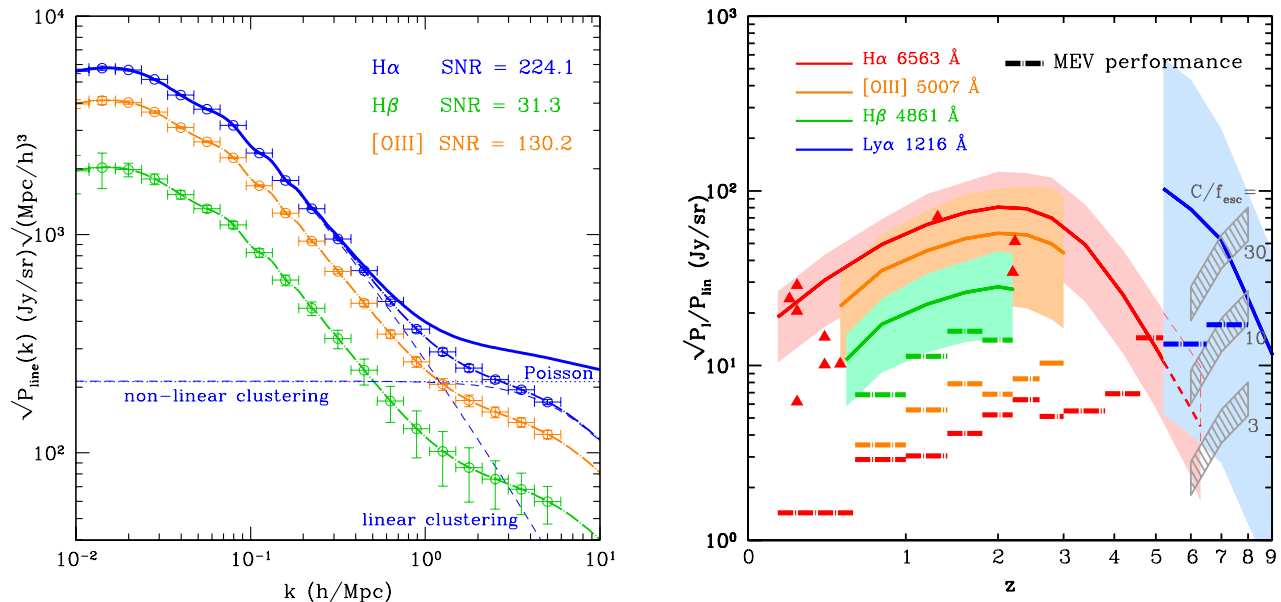


FIG. 25: Left: Three-dimensional power spectrum of the $H\alpha$, $H\beta$ and $[OIII]$ lines at redshift 2. The data points with errors show the statistical uncertainty from the SPHEREx deep survey, which easily detects the linear clustering signal at $k < 1h/\text{Mpc}$, as well as non-linear clustering and Poisson variations at $k > 1h/\text{Mpc}$, with high SNR on the linear clustering amplitude in all 3 lines. Right: SPHEREx will robustly measure the amplitude of linear galaxy clustering in multiple lines over a wide redshift range. The solid curves show the estimated clustering amplitude, in emission lines ($H\alpha$, $H\beta$, $Ly\alpha$ and $[OIII]$) lines with high signal to noise. The MEV performance sensitivity (1σ) is shown by the colored long-dashed lines in redshift bins. SPHEREx will measure $H\alpha$ fluctuations over a wide redshift range $0.2 < z < 6.3$ with high significance throughout. Furthermore, $H\alpha$ and $Ly\alpha$ overlap at $5.2 < z < 6.3$ and can be measured in cross-correlation. At high redshifts, SPHEREx probes $Ly\alpha$ EOR fluctuations that are detectable for models with clustering to escape fractions $C/f_{esc} > 10$.

redshifts may provide an additional probe of reionization [119–122]. The EOR epoch may also be probed by mapping the $Ly\alpha$ line [123, 124]. With SPHEREx sensitivity, $Ly\alpha$ fluctuations are detectable at $S/N \simeq 10$ if the star formation rate density maintains reionization at $z > 6$ (Figure 25). This measurement provides a further consistency test on any EOR component detected in the broad-band measurements described above. Furthermore the line intensity mapping measurement is sensitive to the integrated emission from dwarf galaxies and is thus complementary with JWST surveys that individually resolve galaxies at higher luminosities. Line confusion from lower redshifts requires optimized spectral masking of foreground sources, although we note that the sensitivity in the deep region appears to be sufficient to remove the dominant H contaminant for $Ly\alpha$ EOR studies [124]. We can develop multi-band cross-correlations as an internal check on foreground removal.

XIII. CONCLUSION

In this paper, we introduced the SPHEREx mission and its approach to measuring the three dimensional structure of the Universe. SPHEREx will be the first near-infrared all-sky spectral survey of its kind and will produce an archive of lasting legacy value for the astronomy community. If selected, it will launch in 2020, and nominally acquire data over a two year lifespan, although there are no consumables that preclude a longer lifetime.

While we discussed a few cosmological applications focused on the physics of inflation, it is clear that the 3-D mapping of such an unprecedented cosmological volume would enable numerous other novel cosmological measurements. In the galactic plane, it will exploit the coincidence of its wavelength coverage and the optimal spectral region for ice absorption spectroscopy to resolve long-standing questions about the amount and evolution of such biogenic molecules as H_2O , CO , CO_2 , and CH_3OH through all phases of star and planet formation. The SPHEREx near-infrared all-sky

survey will also enable ground-breaking observations of the extra-galactic background light (EBL).

Appendix A: Biases in large scale structure maps due to redshift errors

Redshift errors introduce two types of errors into a large-scale structure survey [128]. The most familiar such error is the smearing of the density perturbations along the line of sight: like the familiar fingers of God due to true peculiar velocities of galaxies [125], they reduce the observed power spectrum for modes with large k_{\parallel} . There is also a bias in the density perturbation map if the redshift error varies across the sky, due e.g., to variations in sky background and hence in the noise contribution to the observed photometry.

To compute this, let us suppose that there is a true number density of galaxies meeting some threshold $N_g(z, \hat{\mathbf{n}})$, where $\hat{\mathbf{n}}$ denotes a direction on the sky and z the true redshift. This can be re-written as

$$N_g(z, \hat{\mathbf{n}}) = \bar{N}_g(z) [1 + \delta_g(z, \hat{\mathbf{n}})], \quad (\text{A1})$$

where $\delta_g(z, \hat{\mathbf{n}})$ is the density perturbation of the galaxies. Now we suppose that the galaxies are observed with a redshift z_p , whose distribution depends on sky position, i.e., that there exists a $P(z_p|z, \hat{\mathbf{n}})$. Then the observed number of galaxies is

$$N_{g,\text{obs}}(z_p, \hat{\mathbf{n}}) = \int \bar{N}_g(z) [1 + \delta_g(z, \hat{\mathbf{n}})] P(z_p|z, \hat{\mathbf{n}}) dz. \quad (\text{A2})$$

If we expand $P(z_p|z, \hat{\mathbf{n}})$ itself into a sky average and a perturbation,

$$P(z_p|z, \hat{\mathbf{n}}) = \bar{P}(z_p|z) + \delta P(z_p|z, \hat{\mathbf{n}}), \quad (\text{A3})$$

then Eq. (A2) separates into 4 terms:

$$\begin{aligned} N_{g,\text{obs}}(z_p, \hat{\mathbf{n}}) &= \int \bar{N}_g(z) \bar{P}(z_p|z) dz + \int \bar{N}_g(z) \delta_g(z, \hat{\mathbf{n}}) \bar{P}(z_p|z) dz + \int \bar{N}_g(z) \delta P(z_p|z, \hat{\mathbf{n}}) dz \\ &+ \int \bar{N}_g(z) \delta_g(z, \hat{\mathbf{n}}) \delta P(z_p|z, \hat{\mathbf{n}}) dz. \end{aligned} \quad (\text{A4})$$

On large scales (our main interest here), we have $|\delta_g| \ll 1$, and for a well-designed survey we should have $\delta P(z_p|z, \hat{\mathbf{n}})$ small. Thus we will drop the last term, which contains the product of these two, and focus on the leading-order signal terms (the 2nd term) and non-uniformity-induced bias (the 3rd term); the 1st term becomes the survey mean. The observed density fluctuation is then

$$\begin{aligned} \delta_{g,\text{obs}}(z_p, \hat{\mathbf{n}}) &= \frac{N_{g,\text{obs}}(z_p, \hat{\mathbf{n}})}{\bar{N}_{g,\text{obs}}(z_p)} - 1 \\ &= \frac{\int \bar{N}_g(z) \delta_g(z, \hat{\mathbf{n}}) \bar{P}(z_p|z) dz}{\int \bar{N}_g(z) \bar{P}(z_p|z) dz} + \frac{\int \bar{N}_g(z) \delta P(z_p|z, \hat{\mathbf{n}}) dz}{\int \bar{N}_g(z) \bar{P}(z_p|z) dz} \\ &= \int \delta_g(z, \hat{\mathbf{n}}) \bar{P}(z|z_p) dz + \frac{\int \bar{N}_g(z) \delta P(z_p|z, \hat{\mathbf{n}}) dz}{\int \bar{N}_g(z) \bar{P}(z_p|z) dz}. \end{aligned} \quad (\text{A5})$$

In the last line, the first term was simplified using Bayes's theorem. It represents the smoothed density field. The second term, which we will call $\delta_{g,\text{sp}}(z_p, \hat{\mathbf{n}})$, is the spurious large-scale over density field induced by inhomogeneities in survey properties.

The spurious large-scale density perturbation field can be simplified in the case that $P(z_p|z, \hat{\mathbf{n}})$ can be described by a bias $\Delta_z(z, \hat{\mathbf{n}})$ and a scatter $\sigma_z(z, \hat{\mathbf{n}})$. Then we may use the derivative expansion of the probability distribution. Taylor-expanding the expectation value of any function $f(z_p)$ (given z) as

$$\int f(z_p) P(z_p|z, \hat{\mathbf{n}}) dz_p = \langle f(z_p) \rangle|_z = \sum_{j=0}^{\infty} \frac{1}{j!} \langle (z_p - z)^j \rangle|_z f^{(j)}(z) = \sum_{j=0}^{\infty} \frac{1}{j!} \langle (z_p - z)^j \rangle|_z \int f^{(j)}(z_p) \delta(z_p - z) dz_p, \quad (\text{A6})$$

where δ is the Dirac delta function, the superscript (j) indicates a j th derivative and the averages are taken over the probability distribution $P(z_p|z, \hat{\mathbf{n}})$. Integration by parts j times then implies that

$$P(z_p|z, \hat{\mathbf{n}}) = \sum_{j=0}^{\infty} \frac{(-1)^j}{j!} \langle (z_p - z)^j \rangle|_z \delta^{(j)}(z_p - z). \quad (\text{A7})$$

(This should be thought of as an asymptotic expansion; in most cases it does not converge.) Working to order $j = 2$, and using that $\langle (z_p - z)^j \rangle_z = \Delta_z$ (for $j = 1$) or $\sigma_z^2 + \Delta_z^2$ (for $j = 2$), we find

$$P(z_p|z, \hat{\mathbf{n}}) \approx \delta(z_p - z) - \Delta_z(z)\delta'(z_p - z) + \frac{\Delta_z^2(z) + \sigma_z^2(z)}{2}\delta''(z_p - z). \quad (\text{A8})$$

Substituting this into the numerator of the second term in Eq. (A5) – and using the $j = 0$ (trivial) expansion for the denominator – gives

$$\delta_{\text{g,sp}}(z_p, \hat{\mathbf{n}}) = \frac{1}{\bar{N}_g(z_p)} \int \bar{N}_g(z) \left\{ -[\Delta_z(z, \hat{\mathbf{n}}) - \bar{\Delta}_z(z)]\delta'(z_p - z) + \frac{\Delta_z^2(z, \hat{\mathbf{n}}) + \sigma_z^2(z, \hat{\mathbf{n}}) - \bar{\Delta}_z^2(z) - \bar{\sigma}_z^2(z)}{2}\delta''(z_p - z) \right\} dz. \quad (\text{A9})$$

Integrating by parts and simplifying gives

$$\begin{aligned} \delta_{\text{g,sp}}(z_p, \hat{\mathbf{n}}) \approx & \frac{1}{\bar{N}_g(z_p)} \partial_{z_p} \{ [\Delta_z(z_p, \hat{\mathbf{n}}) - \bar{\Delta}_z(z_p)] N_g(z_p) \} \\ & + \frac{1}{2\bar{N}_g(z_p)} \partial_{z_p}^2 \{ [\Delta_z^2(z_p, \hat{\mathbf{n}}) + \sigma_z^2(z_p, \hat{\mathbf{n}}) - \bar{\Delta}_z^2(z_p) - \bar{\sigma}_z^2(z_p)] \bar{N}_g(z_p) \}. \end{aligned} \quad (\text{A10})$$

Equation (A10) gives the general formula for biases in the large scale structure map due to variations in redshift estimation performance. It can be thought of as a “photo- z Eddington bias,” since it involves the change in the observed redshift distribution due to redshift errors (direction-dependent in this case) and – like the original Eddington bias – involves the second derivative of the underlying distribution [126].

A case of special interest is when the redshift bias is small (or has been calibrated out), so that the Δ_z terms may be dropped. However the scatter varies with survey depth, i.e.,

$$\sigma_z(z, \hat{\mathbf{n}}) = \bar{\sigma}_z(z)[1 + \alpha(\hat{\mathbf{n}})], \quad (\text{A11})$$

where $\alpha(\hat{\mathbf{n}})$ is the fractional variation in noise amplitude (i.e., the photometric RMS noise in all bands is $\propto 1 + \alpha$, with $\alpha = 0$ at the survey mean depth, $\alpha > 0$ in shallower regions, and $\alpha < 0$ in deeper regions). We further suppose that the redshift distribution varies faster than the redshift error. (This is a good first approximation for SPHEREx, since the N_g is a rapidly falling function of redshift, and the design of the experiment avoids sharp features in redshift estimation performance as a function of z such as the 4000 Å break redshifting out of the traditional *griz* bands.) Under these approximations, Eq. (A10) reduces to

$$\delta_{\text{g,sp}}(z_p, \hat{\mathbf{n}}) \approx \frac{\bar{N}_g''(z_p)}{\bar{N}_g(z_p)} \alpha(\hat{\mathbf{n}}). \quad (\text{A12})$$

In regions of $\bar{N}_g''(z) > 0$ (such as the falling tail of a redshift distribution), this leads to a positive apparent density fluctuation for RA and Dec with larger noise values, and a negative apparent density fluctuation for RA and Dec with smaller noise values. This dependence on the local noise is used in the systematics budgeting in the main text. There α has been quoted in magnitudes instead of fractional perturbations in the RMS noise: e.g., if $\alpha = 0.01$, then we say that the noise fluctuations are increased by 0.01×1.086 magnitudes.

The spurious large-scale structure power implied by Eq. (A12) is larger than SPHEREx requirements and must be mitigated. Fortunately, like all of the Eddington-like biases, it can be calculated and corrected. In this case, the key is to measure the variation over the sky of the redshift bias and scatter, $\Delta_z(z_p, \hat{\mathbf{n}}) - \bar{\Delta}_z(z_p)$ and $\sigma_z^2(z_p, \hat{\mathbf{n}}) - \bar{\sigma}_z^2(z_p)$. The contribution of increased instrument noise in regions of brighter zodiacal glow to these quantities can be measured by taking low-noise images (near the ecliptic poles), adding artificial noise, and measuring the shift and broadening of the redshift distribution. Note that this is true independent of our knowledge of the absolute bias and scatter $\bar{\Delta}_z(z)$ and $\bar{\sigma}_z^2(z)$.

-
- [1] S. C. Spangelo, R. M. Katti, U. S. C. Unwin, and J. J. Bock (2014), 1412.3142.
 - [2] D. Huterer, S. Shandera, and E. Komatsu, *Adv.Astron.* **2010**, 697147 (2010), 1012.3744.
 - [3] N. Bartolo, E. Komatsu, S. Matarrese, and A. Riotto, *Phys.Rept.* **402**, 103 (2004), astro-ph/0406398.
 - [4] N. Dalal, O. Doré, D. Huterer, and A. Shirokov, *Phys. Rev. D* **77**, 123514 (2008), 0710.4560.
 - [5] K. Abazajian et al. (Topical Conveners: J.E. Carlstrom, A.T. Lee), *Astropart.Phys.* **63**, 55 (2015), 1309.5381.

- [6] M. e. a. Alvarez (2014), 1412.4671.
- [7] D. Salopek and J. Bond, *Phys.Rev.* **D42**, 3936 (1990).
- [8] E. Komatsu, D. N. Spergel, and B. D. Wandelt, *Astrophys.J.* **634**, 14 (2005), astro-ph/0305189.
- [9] Planck Collaboration, P. A. R. Ade, N. Aghanim, C. Armitage-Caplan, M. Arnaud, M. Ashdown, F. Atrio-Barandela, J. Aumont, C. Baccigalupi, A. J. Banday, et al., *Astronomy & Astrophysics* **571**, A24 (2014), 1303.5084.
- [10] C. Bennett et al. (WMAP), *Astrophys.J.Suppl.* **208**, 20 (2013), 1212.5225.
- [11] D. Baumann et al. (CMBPol Study Team), *AIP Conf.Proc.* **1141**, 10 (2009), 0811.3919.
- [12] E. L. Wright, P. R. Eisenhardt, A. Mainzer, M. E. Ressler, R. M. Cutri, et al., *Astron.J.* **140**, 1868 (2010), 1008.0031.
- [13] N. Metcalfe, D. Farrow, S. Cole, P. Draper, P. Norberg, et al., *MNRAS* **435**, **1825-1839** (2013), 1310.6368.
- [14] T. Abbott et al. (Dark Energy Survey Collaboration) (2005), astro-ph/0510346.
- [15] O. Ilbert, P. Capak, M. Salvato, H. Aussel, H. McCracken, et al., *Astrophys.J.* **690**, 1236 (2009), 0809.2101.
- [16] C. Simpson and P. Eisenhardt, *PASP* **111**, 691 (1999), astro-ph/9903067.
- [17] M. Sawicki, *Astron.J.* **124**, 3050 (2002), astro-ph/0209437.
- [18] S. Jouvel, J.-P. Kneib, O. Ilbert, G. Bernstein, S. Arnouts, et al., *Astron.Astrophys.* **504**, 359 (2009), 0902.0625.
- [19] R. J. Cool, J. Moustakas, M. R. Blanton, S. M. Burles, A. L. Coil, et al., *Astrophys.J.* **767**, 118 (2013), 1303.2672.
- [20] P. G. van Dokkum, I. Labbe, D. Marchesini, R. Quadri, G. Brammer, et al. (2009), 0901.0551.
- [21] N. Benitez et al. (J-PAS Collaboration) (2014), 1403.5237.
- [22] P. Mart, R. Miquel, F. J. Castander, E. Gaztaaga, M. Eriksen, et al., *Mon.Not.Roy.Astron.Soc.* **442**, 92 (2014), 1402.3220.
- [23] D. Lang, D. W. Hogg, K. Mierle, M. Blanton, and S. Roweis, *Astron.J.* **139**, 1782 (2010), 0910.2233.
- [24] P. M. Korngut, T. Renbarger, T. Arai, J. Battle, J. Bock, S. W. Brown, A. Cooray, V. Hristov, B. Keating, M. G. Kim, et al., *ApJS* **207**, 34 (2013), 1307.0016.
- [25] K. Tsumura, T. Arai, J. Battle, J. Bock, S. Brown, A. Cooray, V. Hristov, B. Keating, M. G. Kim, D. H. Lee, et al., *ApJS* **207**, 33 (2013), 1112.4217.
- [26] M. Zemcov, T. Arai, J. Battle, J. Bock, A. Cooray, V. Hristov, B. Keating, M. G. Kim, D. H. Lee, L. R. Levenson, et al., *ApJS* **207**, 31 (2013), 1112.1424.
- [27] P. McDonald and U. Seljak, *JCAP* **0910**, 007 (2009), 0810.0323.
- [28] C. Blake, I. K. Baldry, J. Bland-Hawthorn, L. Christodoulou, M. Colless, C. J. Conselice, S. P. Driver, A. M. Hopkins, J. Liske, J. Loveday, et al. (2013), 1309.5556, URL <http://arxiv.org/abs/1309.5556>.
- [29] M. Tegmark, A. Taylor, and A. Heavens, *Astrophys.J.* **480**, 22 (1997).
- [30] U. Seljak, *Physical Review Letters* **102**, 021302 (2009), 0807.1770.
- [31] N. Hamaus, U. Seljak, and V. Desjacques, *Phys. Rev. D* **86**, 103513 (2012), 1207.1102.
- [32] R. de Putter and O. Doré (2014), 1412.3854.
- [33] S. Matarrese and L. Verde, *ApJL* **677**, L77 (2008), 0801.4826.
- [34] A. Slosar, C. Hirata, U. Seljak, S. Ho, and N. Padmanabhan, *JCAP* **8**, 031 (2008), 0805.3580.
- [35] V. Desjacques and U. Seljak, *Classical and Quantum Gravity* **27**, 124011 (2010), 1003.5020.
- [36] A. Leauthaud, J. Tinker, K. Bundy, P. S. Behroozi, R. Massey, J. Rhodes, M. R. George, J.-P. Kneib, A. Benson, R. H. Wechsler, et al., *ApJ* **744**, 159 (2012), 1104.0928.
- [37] J. Tinker, A. V. Kravtsov, A. Klypin, K. Abazajian, M. Warren, G. Yepes, S. Gottlöber, and D. E. Holz, *ApJ* **688**, 709 (2008), 0803.2706.
- [38] J. L. Tinker, B. E. Robertson, A. V. Kravtsov, A. Klypin, M. S. Warren, G. Yepes, and S. Gottlöber, *ApJ* **724**, 878 (2010), 1001.3162.
- [39] H.-J. Seo and D. J. Eisenstein, *ApJ* **665**, 14 (2007), arXiv:astro-ph/0701079.
- [40] R. Ellis, M. Takada, H. Aihara, N. Arimoto, K. Bundy, M. Chiba, J. Cohen, O. Dore, J. E. Greene, J. Gunn, et al., *ArXiv e-prints* (2012), 1206.0737.
- [41] N. Kaiser, *Mon.Not.Roy.Astron.Soc.* **227**, 1 (1987).
- [42] J. Asorey, M. Crocce, E. Gaztañaga, and A. Lewis, *Mon. Not. R. Astron. Soc.* **427**, 1891 (2012), 1207.6487.
- [43] D. J. Eisenstein, H.-J. Seo, E. Sirko, and D. N. Spergel, *ApJ* **664**, 675 (2007), arXiv:astro-ph/0604362.
- [44] N. Padmanabhan, X. Xu, D. J. Eisenstein, R. Scalzo, A. J. Cuesta, K. T. Mehta, and E. Kazin, *Mon. Not. R. Astron. Soc.* **427**, 2132 (2012), 1202.0090.
- [45] A. Lewis, A. Challinor, and A. Lasenby, *Astrophys.J.* **538**, 473 (2000), arXiv:astro-ph/9911177.
- [46] H. Gil-Marn, L. Verde, J. Norea, A. J. Cuesta, L. Samushia, et al. (2014), 1408.0027.
- [47] H. Gil-Marn, J. Norea, L. Verde, W. J. Percival, C. Wagner, et al. (2014), 1407.5668.
- [48] D. Jeong, Ph.D. thesis, University of Texas at Austin (2010).
- [49] Planck Collaboration, P. A. R. Ade, N. Aghanim, C. Armitage-Caplan, M. Arnaud, M. Ashdown, F. Atrio-Barandela, J. Aumont, C. Baccigalupi, A. J. Banday, et al., *ArXiv e-prints* (2013), 1303.5076.
- [50] L. Anderson, É. Aubourg, S. Bailey, F. Beutler, V. Bhardwaj, M. Blanton, A. S. Bolton, J. Brinkmann, J. R. Brownstein, A. Burden, et al., *Mon. Not. R. Astron. Soc.* **441**, 24 (2014), 1312.4877.
- [51] J. Maldacena, *Journal of High Energy Physics* **5**, 013 (2003), astro-ph/0210603.
- [52] P. Creminelli and M. Zaldarriaga, *JCAP* **10**, 006 (2004), astro-ph/0407059.
- [53] D. H. Lyth, C. Ungarelli, and D. Wands, *Phys. Rev. D* **67**, 023503 (2003), astro-ph/0208055.
- [54] M. Zaldarriaga, *Phys. Rev. D* **69**, 043508 (2004), astro-ph/0306006.
- [55] F. Schmidt and M. Kamionkowski, *Phys. Rev. D* **82**, 103002 (2010), 1008.0638.
- [56] V. Desjacques, D. Jeong, and F. Schmidt, *Phys. Rev. D* **84**, 061301 (2011), 1105.3476.

- [57] A. R. Pullen and C. M. Hirata, *Publications of the Astronomical Society of the Pacific*, Volume 125, Issue 928, pp. **705-718** (2013), 1212.4500.
- [58] K. Tsumura, T. Matsumoto, S. Matsuura, I. Sakon, M. Tanaka, and T. Wada, *PASJ* **65**, 120 (2013), 1307.6736.
- [59] K. Tsumura, J. Battle, J. Bock, A. Cooray, V. Hristov, et al., *Astrophys.J.* **719**, 394 (2010), 1004.5445.
- [60] E. M. Huff, T. Eifler, C. M. Hirata, R. Mandelbaum, D. Schlegel, et al. (2011), 1112.3143.
- [61] T. Kelsall, J. Weiland, B. Franz, W. Reach, R. Arendt, et al., *Astrophys.J.* **508**, 44 (1998), astro-ph/9806250.
- [62] M. A. Strauss et al. (SDSS Collaboration), *Astron.J.* **124**, 1810 (2002), astro-ph/0206225.
- [63] J. Bock, I. Sullivan, T. Arai, J. Battle, A. Cooray, et al., *Astrophys.J.Suppl.* **207**, 32 (2013), 1206.4702.
- [64] e. a. Barker, E.A., STSI WFC3 Instr. Sci. Report, 200940 (2009).
- [65] e. a. Russell, JWST investigation, JWST-STScI-001650, SM-12 **SM-12** (2009).
- [66] e. a. Robberto, M., AAS Meeting 217, 254.20 **217** (2011).
- [67] e. a. Russell, R., SPIE, 7021, 12 **7021** (2008).
- [68] R. Laureijs, J. Amiaux, S. Arduini, J. . Auguères, J. Brinchmann, R. Cole, M. Cropper, C. Dabin, L. Duvet, A. Ealet, et al., *ArXiv e-prints* (2011), 1110.3193.
- [69] D. Spergel, N. Gehrels, J. Breckinridge, M. Donahue, A. Dressler, B. S. Gaudi, T. Greene, O. Guyon, C. Hirata, J. Kalirai, et al., *ArXiv e-prints* (2013), 1305.5422.
- [70] J. A. Newman, *ApJ* **684**, 88 (2008), 0805.1409.
- [71] R. de Putter, O. Doré, and S. Das, *ArXiv e-prints* (2013), 1306.0534.
- [72] B. Ménard, R. Scranton, S. Schmidt, C. Morrison, D. Jeong, T. Budavari, and M. Rahman, *ArXiv e-prints* (2013), 1303.4722.
- [73] G. Bernstein and D. Huterer, *Mon. Not. R. Astron. Soc.* **401**, 1399 (2010), 0902.2782.
- [74] B. Joachimi, R. Mandelbaum, F. B. Abdalla, and S. L. Bridle, *A&A* **527**, A26 (2011), 1008.3491.
- [75] R. Mandelbaum, C. Blake, S. Bridle, F. B. Abdalla, S. Brough, M. Colless, W. Couch, S. Croom, T. Davis, M. J. Drinkwater, et al., *Mon. Not. R. Astron. Soc.* **410**, 844 (2011), 0911.5347.
- [76] A. R. Zentner, E. Semboloni, S. Dodelson, T. Eifler, E. Krause, and A. P. Hearin, *Phys. Rev. D* **87**, 043509 (2013), 1212.1177.
- [77] T. Eifler, E. Krause, S. Dodelson, A. Zentner, A. Hearin, and N. Gnedin, *ArXiv* 1405.7423 (2014), 1405.7423.
- [78] B. Joachimi and S. L. Bridle, *A&A* **523**, A1 (2010), 0911.2454.
- [79] T. Eifler, E. Krause, P. Schneider, and K. Honscheid, *Mon. Not. R. Astron. Soc.* **440**, 1379 (2014), 1302.2401.
- [80] R. Reyes, R. Mandelbaum, U. Seljak, T. Baldauf, J. E. Gunn, L. Lombriser, and R. E. Smith, *Nature* **464**, 256 (2010), 1003.2185.
- [81] P. Simon, P. Schneider, and D. Kübler, *A&A* **548**, A102 (2012), 1202.1927.
- [82] P. Simon, T. Erben, P. Schneider, C. Heymans, H. Hildebrandt, H. Hoekstra, T. D. Kitching, Y. Mellier, L. Miller, L. Van Waerbeke, et al., *Mon. Not. R. Astron. Soc.* **430**, 2476 (2013), 1301.1863.
- [83] A. Raccanelli, D. Bertacca, R. Maartens, C. Clarkson, and O. Doré (2013), 1311.6813.
- [84] A. Raccanelli, D. Bertacca, O. Doré, and R. Maartens, *JCAP* **1408**, 022 (2014), 1306.6646.
- [85] J. Coupon, M. Kilbinger, H. McCracken, O. Ilbert, S. Arnouts, et al., *Astron.Astrophys.* **542**, A5 (2012), 1107.0616.
- [86] N. P. Ross, I. D. McGreer, M. White, G. T. Richards, A. D. Myers, et al., *Astrophys.J.* **773**, 14 (2013), 1210.6389.
- [87] J. E. Geach, D. N. Murphy, and R. G. Bower, *Mon.Not.Roy.Astron.Soc.* **413**, 3059 (2011), 1101.4585.
- [88] K. I. Oberg, N. van der Marel, L. E. Kristensen, and E. F. van Dishoeck, *Astrophys.J.* **740**, 14 (2011), 1107.5824.
- [89] P. Caselli, E. Keto, E. A. Bergin, M. Tafalla, Y. Aikawa, et al. (2012), 1208.5998.
- [90] N. Sakai, T. Sakai, T. Hirota, and S. Yamamoto, *ApJ* **672**, 371 (2008).
- [91] M. R. Hogerheijde, E. A. Bergin, C. Brinch, L. I. Cleeves, J. K. Fogel, et al., *Science* **334**, 338 (2011), 1110.4600.
- [92] L. I. Cleeves, E. A. Bergin, C. M. O. . Alexander, F. Du, D. Graninger, K. I. Öberg, and T. J. Harries, *Science* **345**, 1590 (2014), 1409.7398.
- [93] K. M. Pontoppidan, C. P. Dullemond, E. F. van Dishoeck, G. A. Blake, A. C. Boogert, et al., *Astrophys.J.* **622**, 463 (2005), astro-ph/0411367.
- [94] Y. Aikawa, V. Wakelam, F. Hersant, R. T. Garrod, and E. Herbst, *Astrophys.J.* **760**, 40 (2012), 1210.2476.
- [95] M. Skrutskie, R. Cutri, R. Stiening, M. Weinberg, S. Schneider, et al., *Astron.J.* **131**, 1163 (2006).
- [96] S. R. Majewski, G. Zasowski, and D. L. Nidever, *Astrophys.J.* **739**, 25 (2011), 1106.2542.
- [97] J. Noble, H. Fraser, Y. Aikawa, K. Pontoppidan, and I. Sakon, *Astrophys.J.* **775**, 85 (2013), 1307.1527.
- [98] E. L. Gibb, D. C. B. Whittet, A. C. A. Boogert, and A. G. G. M. Tielens, *ApJS* **151**, 35 (2004).
- [99] K. I. Oberg, C. Qi, J. K. Fogel, E. A. Bergin, S. M. Andrews, et al., *Astrophys.J.* **734**, 98 (2011), 1104.1236.
- [100] A. G. G. M. Tielens and W. Hagen, *A&A* **114**, 245 (1982).
- [101] H. Cuppen, E. van Dishoeck, E. Herbst, and A. Tielens, *Astron.Astrophys.* **508**, 275 (2009), 0911.0283.
- [102] R. T. Garrod, S. L. W. Weaver, and E. Herbst, *Astrophys.J.* **682**, 283 (2008), 0803.1214.
- [103] K. Oberg, R. Garrod, E. van Dishoeck, and H. Linnartz, *Astron.Astrophys.* **504**, 891 (2009), 0908.1169.
- [104] R. Visser, E. van Dishoeck, S. Doty, and C. Dullemond, *Astron.Astrophys.* **495**, 881 (2009), 0901.1313.
- [105] M. Mumma, B. Bonev, G. Villanueva, L. Paganini, M. DiSanti, et al., *Astrophys.J.* **734**, L7 (2011), 1104.4665.
- [106] C. Qi, K. I. Oberg, D. J. Wilner, P. d'Alessio, E. Bergin, et al. (2013), 1307.7439.
- [107] J. Drażkowska and C. P. Dullemond, *A&A* **572**, A78 (2014), 1410.3832.
- [108] K. I. Oberg, C. Qi, D. J. Wilner, and S. M. Andrews, *Astrophys.J.* **743**, 152 (2011), 1109.2578.
- [109] T. Matsumoto, H. Seo, W.-S. Jeong, H. Lee, S. Matsuura, et al., *Astrophys.J.* **742**, 124 (2011), 1010.0491.

- [110] A. Kashlinsky, R. Arendt, J. C. Mather, and S. Moseley, *Nature* **438**, 45 (2005), astro-ph/0511105.
 - [111] A. Cooray, Y. Gong, J. Smidt, and M. G. Santos, *Astrophys.J.* **756**, 92 (2012), 1205.2316.
 - [112] M. Zemcov, J. Smidt, T. Arai, J. Bock, A. Cooray, et al., *Science* **346**, 732 (2014), 1411.1411.
 - [113] K. Helgason, M. Ricotti, and A. Kashlinsky, *Astrophys.J.* **752**, 113 (2012), 1201.4398.
 - [114] N. Cappelluti, A. Kashlinsky, R. Arendt, A. Comastri, G. Fazio, et al., *Astrophys.J.* **769**, 68 (2013), 1210.5302.
 - [115] B. Yue, A. Ferrara, R. Salvaterra, Y. Xu, and X. Chen, *Mon.Not.Roy.Astron.Soc.* **433**, 1556 (2013), 1305.5177.
 - [116] R. Bouwens, G. Illingworth, P. Oesch, I. Labbe, P. van Dokkum, et al., *Astrophys.J.* **793**, 115 (2014), 1306.2950.
 - [117] T. Tal and P. van Dokkum, *Astrophys.J.* **731**, 89 (2011), 1102.4330.
 - [118] A. Cooray, J. Smidt, F. De Bernardis, Y. Gong, D. Stern, et al., *Nature* **494**, 514 (2012), 1210.6031.
 - [119] Y. Gong, A. Cooray, and M. G. Santos, *Astrophys.J.* **768**, 130 (2013), 1212.2964.
 - [120] Y. Gong, X. Chen, M. Silva, A. Cooray, and M. G. Santos, *Astrophys.J.* **740**, L20 (2011), 1108.0947.
 - [121] A. Lidz, S. R. Furlanetto, S. P. Oh, J. Aguirre, T.-C. Chang, et al., *Astrophys.J.* **741**, 70 (2011), 1104.4800.
 - [122] E. Visbal and A. Loeb, *JCAP* **1011**, 016 (2010), 1008.3178.
 - [123] M. Silva, M. G. Santos, Y. Gong, and A. Cooray, *Astrophys.J.* **763**, 132 (2013), 1205.1493.
 - [124] A. R. Pullen, O. Dore, and J. Bock, *Astrophys.J.* **786**, 111 (2014), 1309.2295.
 - [125] J. C. Jackson, *Mon. Not. R. Astron. Soc.* **156**, 1P (1972).
 - [126] A. S. Eddington, *Mon. Not. R. Astron. Soc.* **73**, 359 (1913).
 - [127] <http://www.stsci.edu/jwst/instruments/nircam/docarchive/JWST-STScI-001650.pdf>
 - [128] The same variations in photometry that lead to spatially varying redshift errors may also lead to spurious clustering by pushing galaxies over the threshold defining the sample (e.g. a signal-to-noise cut), i.e. by modulating the selection function. This well studied effect is not included in this Appendix.
-